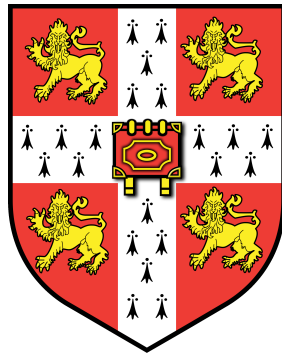


Exploring Gravity With Gravitational Waves & Strong-Field Tests

Christopher Berry

Churchill College
and
Institute of Astronomy,
University of Cambridge

Supervisor: Jonathan Gair



Certificate of Postgraduate Study

1 September 2010

Chapter 1

Introduction

1.1 Gravitation

Gravity is one of the fundamental forces of nature; familiar as the force that keeps the Earth in orbit about the Sun, causes apples to fall from trees, and makes falling off a log so easy. Yet there is much we do not know about gravity. We do not have a complete quantum theory, or even a definite framework to find one. Modern physics describes gravity using the classical theory of general relativity (GR)^[1]. Since its inception by Einstein in 1915 GR has successfully passed every observational test^[2]. However, these tests have primarily focused on weak gravitational fields. Strong gravitational fields provide more interesting tests: because gravity is stronger any correction to GR should be more noticeable. This effect is amplified because gravitation is non-linear. Strong fields are found in regions of high spacetime curvature, such as in the areas surrounding massive compact objects (COs), like black holes (BHs) or neutron stars (NSs).

One particularly promising method of exploring strong-field regions would be to observe gravitational waves (GWs), allowing us to probe gravitational interactions in regimes that are currently inaccessible using more traditional, electromagnetic observations. For example, binary encounters between massive COs create gravitational fields both intensely strong and highly dynamical, a domain where GR has yet to be tested. As yet no GWs have been directly detected, although their existence has been inferred from the loss of energy and angular momentum from binary pulsars^[3]. There are a number of experiments designed to measure gravitational radiation: the ground-based detectors of the Laser Interferometer Gravitational-Wave Observatory (LIGO)^[4, 5] and Virgo^[6] collaboration may be the first to see GWs, but of particular interest for many astrophysical applications is the planned NASA/ESA Laser Interferometer Space Antenna (LISA)^[7, 8]. Observing GWs would allow us to learn about the systems that generate them.

While GWs are an exciting source of information, it will be beneficial to compare with results from other techniques, to maximise the data available for inferences, and to check models. For example, very long baseline interferometry (VLBI) may be used to image the vicinity of a BH's horizon, or X-ray observations could be used to investigate BH accretion discs^[9].

This work investigates what we might be able to learn about gravity and massive COs through a variety of strong-field and weak-field tests, with emphasis upon GWs.

1.2 Structure

In chapter 2 we examine an alternative theory of gravity: metric $f(R)$. We focus on the modifications to gravitational radiation and possible observational tests that may be used to constrain the theory. Many of the results are already known in the literature, but are worked out here *ab initio*. We include them as a compendium of useful results, within a consistent system of notation, and to highlight some important points. Seemingly new results are found in section 2.4.4.

In chapter 3 we investigate what might be inferred by observing gravitational radiation from an object on a highly eccentric orbit about the galactic centre. Waveform construction, signal analysis and parameter estimation are discussed, and some preliminary results are presented.

Finally in chapter 4 we outline further areas of interest that may be studied in the future.

1.3 Conventions

Throughout this work we will use the time-like sign convention of Landau and Lifshitz^[10]:

1. The metric has signature $(+, -, -, -)$.
2. The Riemann tensor is defined as $R^\mu_{\nu\sigma\rho} = \partial_\sigma \Gamma^\mu_{\nu\rho} - \partial_\rho \Gamma^\mu_{\nu\sigma} + \Gamma^\mu_{\lambda\sigma} \Gamma^\lambda_{\rho\nu} - \Gamma^\mu_{\lambda\rho} \Gamma^\lambda_{\sigma\nu}$.
3. The Ricci tensor is defined as the contraction $R_{\mu\nu} = R^\lambda_{\mu\lambda\nu}$.

Greek indices are used to represent spacetime indices $\mu = \{0, 1, 2, 3\}$ and lowercase Latin indices from the middle of the alphabet are used for spatial indices $i = \{1, 2, 3\}$. Uppercase Latin indices from the beginning of the alphabet will be used for the output of two LISA detector-arms $A = \{I, II\}$, and lowercase Latin indices from the beginning of the alphabet are used for parameter space. Summation over repeated indices is assumed unless explicitly noted otherwise. Geometric units with $G = c = 1$ will be used where noted, but in general factors of G and c will be retained.

Chapter 2

Gravitational Radiation In $f(R)$ Theory

2.1 Introduction To $f(R)$ Theory

General relativity is a well tested theory of gravity^[2]; however it is still interesting to explore alternative theories. This can be motivated by the need to explain dark matter and dark energy in cosmology, trying to formulate a quantizable theory of gravity, or simple curiosity regarding the uniqueness of GR. One of the simplest extensions to standard GR is the class of $f(R)$ theories^[11,12].

2.1.1 The Action & Field Equations

General relativity may be derived from the Einstein-Hilbert action^[1,10]

$$S_{\text{EH}}[g] = \frac{c^4}{16\pi G} \int R \sqrt{-g} \, d^4x. \quad (2.1)$$

In $f(R)$ theory we make a simple modification of the action to include an arbitrary function of the Ricci scalar R such that^[13]

$$S[g] = \frac{c^4}{16\pi G} \int f(R) \sqrt{-g} \, d^4x. \quad (2.2)$$

Including the function $f(R)$ gives extra freedom in defining the behaviour of gravity; while this action may not encode the true theory of gravity it may at least contain sufficient information to act as an effective field theory, correctly describing phenomenological behaviour^[14]. We will assume that $f(R)$ is analytic about $R = 0$ so that it may be expressed as a power series^[9,13]

$$f(R) = a_0 + a_1 R + \frac{a_2}{2!} R^2 + \frac{a_3}{3!} R^3 + \dots \quad (2.3)$$

Since the dimensions of $f(R)$ must be the same as of R , $[a_n] = [R]^{(1-n)}$. To link to GR we will set $a_1 = 1$; any rescaling may be absorbed into the definition of G .

The field equations are obtained by a variational principle; there are several ways of achieving this. To derive the Einstein field equations from the Einstein-Hilbert action one may use the standard metric variation or the Palatini variation^[1]. Both approaches may be used for $f(R)$, however they yield different results^[11,12]. Following the metric formalism, one varies the action with respect to the metric $g^{\mu\nu}$, the resulting field equations being for metric $f(R)$ -gravity. Following the Palatini formalism one varies the action with respect to both the metric $g^{\mu\nu}$ and the connection $\Gamma^\rho_{\mu\nu}$, which are treated as independent quantities: the connection is not the Levi-Civita metric connection.¹

Finally, there is a third version of $f(R)$ -gravity: metric-affine $f(R)$ -gravity^[19,20]. This goes beyond the Palatini formalism by supposing that the matter action is dependent on the variational independent connection. Parallel transport and the covariant derivative are divorced from the metric. This theory has its attractions: it allows for a natural introduction of torsion. However, it is not a metric theory of gravity and so cannot satisfy all the postulates of the Einstein equivalence principle^[2]: a free particle does not necessarily follow a geodesic and so the effects of gravity might not be locally removed^[15]. The implications of this have not been fully explored, but for this reason we shall not consider the theory further.

We shall restrict our attention to metric $f(R)$ -gravity. This is preferred as the Palatini formalism has undesirable properties: static spherically symmetric objects described by a polytropic equation of state are subject to a curvature singularity^[21,22]. Varying the action with respect to the metric $g^{\mu\nu}$ produces

$$\delta S = \frac{c^4}{16\pi G} \int \left\{ f'(R) \sqrt{-g} [R_{\mu\nu} - \nabla_\mu \nabla_\nu + g_{\mu\nu} \square] - f(R) \frac{1}{2} \sqrt{-g} g_{\mu\nu} \right\} \delta g^{\mu\nu} d^4x, \quad (2.4)$$

where $\square = g^{\mu\nu} \nabla_\mu \nabla_\nu$ is the d'Alembertian and a prime denotes differentiation with respect to R . Proceeding from here requires certain assumptions regarding surface terms. In the case of the Einstein-Hilbert action these gather into a total derivative. It is possible to subtract this from the action to obtain a well-defined variational quantity^[23,24]. This is not the case for general $f(R)$ ^[25]. However, since the action includes higher-order derivatives of the metric we are at liberty to fix more degrees of freedom at the boundary, in so doing eliminating the importance of the surface terms^[11,26]. There is no well described prescription for this so we proceed directly to the field equations.

The vacuum field equations are

$$f' R_{\mu\nu} - \nabla_\mu \nabla_\nu f' + g_{\mu\nu} \square f' - \frac{f}{2} g_{\mu\nu} = 0. \quad (2.5)$$

Taking the trace of our field equation gives

$$f' R + 3 \square f' - 2f = 0. \quad (2.6)$$

¹Requiring that the metric and Palatini formalisms produce the same field equations, assuming an action that only depends on the metric and Riemann tensor, results in Lovelock gravity^[15]. Lovelock gravities require the field equations to be divergence free and no more than second order; in four dimensions the only possible Lovelock gravity is GR with a potentially non-zero cosmological constant^[16–18].

If we consider a uniform flat spacetime $R = 0$, this equation gives

$$a_0 = 0. \quad (2.7)$$

In analogy to the Einstein tensor, we shall define

$$\mathcal{G}_{\mu\nu} = f' R_{\mu\nu} - \nabla_\mu \nabla_\nu f' + g_{\mu\nu} \square f' - \frac{f}{2} g_{\mu\nu}, \quad (2.8)$$

so that in a vacuum

$$\mathcal{G}_{\mu\nu} = 0. \quad (2.9)$$

2.1.2 Conservation Of Energy-Momentum

If we introduce matter with a stress-energy tensor $T_{\mu\nu}$, the field equations become

$$\mathcal{G}_{\mu\nu} = \frac{8\pi G}{c^4} T_{\mu\nu}. \quad (2.10)$$

If we act upon this with the covariant derivative we obtain

$$\begin{aligned} \frac{8\pi G}{c^4} \nabla^\mu T_{\mu\nu} &= \nabla^\mu \mathcal{G}_{\mu\nu} \\ &= R_{\mu\nu} \nabla^\mu f' + f' \nabla^\mu \left(R_{\mu\nu} - \frac{1}{2} R g_{\mu\nu} \right) - (\square \nabla_\nu - \nabla_\nu \square) f'. \end{aligned} \quad (2.11)$$

The second term contains the covariant derivative of the Einstein tensor and so is zero. The final term can be shown to be

$$\begin{aligned} (\square \nabla_\nu - \nabla_\nu \square) f' &= g^{\mu\sigma} [\nabla_\mu \nabla_\sigma \nabla_\nu - \nabla_\nu \nabla_\mu \nabla_\sigma] f' \\ &= R_{\tau\nu} \nabla^\tau f', \end{aligned} \quad (2.12)$$

which is a useful geometric identity^[27]. Using this

$$\begin{aligned} \frac{8\pi G}{c^4} \nabla^\mu T_{\mu\nu} &= R_{\mu\nu} \nabla^\mu f' - R_{\mu\nu} \nabla^\mu f' \\ &= 0. \end{aligned} \quad (2.13)$$

Consequently energy-momentum is a conserved quantity in the same way as in GR, as may be expected from the symmetries of the action.

2.2 Linearized Theory

We will start our investigation of $f(R)$ by looking at linearized theory. This is a weak-field approximation that assumes only small deviations from a flat background, greatly simplifying the field equations. Just as in GR, the linearized framework provides a natural way to study gravitational waves. We will see that the linearized field equations will reduce down to flat-space wave equations: GWs are as much a part of $f(R)$ -gravity as of GR.

Consider the case that the metric is perturbed slightly from flat Minkowski space such that

$$g_{\mu\nu} = \eta_{\mu\nu} + h_{\mu\nu}; \quad (2.14)$$

where, more formally, we mean that $h_{\mu\nu} = \varepsilon H_{\mu\nu}$ for a small parameter ε .² We will consider terms only to $\mathcal{O}(\varepsilon)$. Thus, the inverse metric is

$$g^{\mu\nu} = \eta^{\mu\nu} - h^{\mu\nu}, \quad (2.15)$$

where we have used the Minkowski metric to raise the indices on the right, defining

$$h^{\mu\nu} = \eta^{\mu\sigma} \eta^{\nu\rho} h_{\sigma\rho}. \quad (2.16)$$

Similarly, the trace h is given by

$$h = \eta^{\mu\nu} h_{\mu\nu}. \quad (2.17)$$

All quantities denoted by “ h ” are strictly $\mathcal{O}(\varepsilon)$.

The linearized connection is

$$\Gamma^{(1)\rho}_{\mu\nu} = \frac{1}{2} \eta^{\rho\lambda} (\partial_\mu h_{\lambda\nu} + \partial_\nu h_{\lambda\mu} - \partial_\lambda h_{\mu\nu}). \quad (2.18)$$

To $\mathcal{O}(\varepsilon)$ the covariant derivative of any perturbed quantity will be the same as the partial derivative. The Riemann tensor is

$$R^{(1)\lambda}_{\mu\nu\rho} = \frac{1}{2} (\partial_\mu \partial_\nu h_\rho^\lambda + \partial^\lambda \partial_\rho h_{\mu\nu} - \partial_\mu \partial_\rho h_\nu^\lambda - \partial^\lambda \partial_\nu h_{\mu\rho}), \quad (2.19)$$

where we have raised the index on the differential operator with the background Minkowski metric. Contracting gives the Ricci tensor

$$R^{(1)}_{\mu\nu} = \frac{1}{2} (\partial_\mu \partial_\rho h_\nu^\rho + \partial_\nu \partial_\rho h_\mu^\rho - \square h_{\mu\nu} - \partial_\mu \partial_\nu h), \quad (2.20)$$

where the d'Alembertian operator is $\square = \eta^{\mu\nu} \partial_\mu \partial_\nu$. Contracting this with $\eta^{\mu\nu}$ gives the first order Ricci scalar

$$R^{(1)} = \partial_\mu \partial_\rho h^{\rho\mu} - \square h. \quad (2.21)$$

Since $R^{(1)}$ is $\mathcal{O}(\varepsilon)$ we may write $f(R)$ as a Maclaurin series to first order such that

$$f(R) = a_0 + R^{(1)}; \quad (2.22)$$

$$f'(R) = 1 + a_2 R^{(1)}. \quad (2.23)$$

As we are perturbing from a Minkowski background where the Ricci scalar vanishes, we may use equation (2.7) to set $a_0 = 0$. Inserting these into equation (2.8) and retaining terms to $\mathcal{O}(\varepsilon)$ yields

$$\mathcal{G}^{(1)}_{\mu\nu} = R^{(1)}_{\mu\nu} - \partial_\mu \partial_\nu (a_2 R^{(1)}) + \eta_{\mu\nu} \square (a_2 R^{(1)}) - \frac{R^{(1)}}{2} \eta_{\mu\nu}. \quad (2.24)$$

²It is because we wish to perturb about flat spacetime that we have required $f(R)$ to be analytic about $R = 0$.

We need to find a relation between $R^{(1)}$ and its derivatives; let us consider the linearized trace equation, from equation (2.6)

$$\begin{aligned}\mathcal{G}^{(1)} &= R^{(1)} + 3\Box(a_2 R^{(1)}) - 2R^{(1)} \\ \mathcal{G}^{(1)} &= 3a_2\Box R^{(1)} - R^{(1)},\end{aligned}\tag{2.25}$$

where $\mathcal{G}^{(1)} = \eta^{\mu\nu}\mathcal{G}^{(1)}_{\mu\nu}$. This is the massive inhomogeneous Klein-Gordon equation. Setting $\mathcal{G} = 0$, as for a vacuum, we obtain the standard Klein-Gordon equation

$$\Box R^{(1)} + \Upsilon^2 R^{(1)} = 0,\tag{2.26}$$

defining the reciprocal length (squared)

$$\Upsilon^2 = -\frac{1}{3a_2}.\tag{2.27}$$

For a physically meaningful solution $\Upsilon^2 > 0$, thus we constrain $f(R)$ such that $a_2 < 0$ ^[28–31]. From Υ we may define a reduced Compton wavelength

$$\lambda_R = \frac{1}{\Upsilon},\tag{2.28}$$

and mass

$$m_R = \frac{\hbar\Upsilon}{c}\tag{2.29}$$

associated with this scalar mode.

The next step is to substitute in $h_{\mu\nu}$ to try to find wave solutions. We want a quantity $\bar{h}_{\mu\nu}$ that will satisfy a wave equation, related to $h_{\mu\nu}$ by

$$\bar{h}_{\mu\nu} = h_{\mu\nu} + A_{\mu\nu}.\tag{2.30}$$

In GR we use the trace-reversed form where $A_{\mu\nu} = -(h/2)\eta_{\mu\nu}$. This will not suffice here, but let us look for a similar solution

$$\bar{h}_{\mu\nu} = h_{\mu\nu} - \frac{h}{2}\eta_{\mu\nu} + B_{\mu\nu}.\tag{2.31}$$

The only rank two tensors in our theory are: $h_{\mu\nu}$, $\eta_{\mu\nu}$, $R^{(1)}_{\mu\nu}$, and $\partial_\mu\partial_\nu$; $h_{\mu\nu}$ has been used already, and we wish to eliminate $R^{(1)}_{\mu\nu}$, so we will try the simpler option based around $\eta_{\mu\nu}$. We want $B_{\mu\nu}$ to be $\mathcal{O}(\varepsilon)$. There are three scalar quantities that satisfy this: h , $R^{(1)}$ and $\Box R^{(1)}$; h is used already and $\Box R^{(1)}$ is related to $R^{(1)}$ by equation (2.25). Therefore, we may construct an ansatz

$$\bar{h}_{\mu\nu} = h_{\mu\nu} + \left(ba_2 R^{(1)} - \frac{h}{2}\right)\eta_{\mu\nu},\tag{2.32}$$

where a_2 has been included to ensure dimensional consistency and b is a dimensionless number. Contracting with the background metric yields

$$\bar{h} = 4ba_2 R^{(1)} - h,\tag{2.33}$$

so we may eliminate h in our definition of $\bar{h}_{\mu\nu}$ to give

$$h_{\mu\nu} = \bar{h}_{\mu\nu} + \left(ba_2 R^{(1)} - \frac{\bar{h}}{2} \right) \eta_{\mu\nu}. \quad (2.34)$$

Just as in GR, we have the freedom to perform a gauge transformation^[1,32]: the field equations are gauge invariant since we started with a function of the gauge invariant Ricci scalar. We will assume a Lorenz, or de Donder, gauge choice so

$$\nabla^\mu \bar{h}_{\mu\nu} = 0; \quad (2.35)$$

to first order this is

$$\partial^\mu \bar{h}_{\mu\nu} = 0. \quad (2.36)$$

Subject to this, from equation (2.20), the Ricci tensor is

$$R^{(1)}_{\mu\nu} = -\frac{1}{2} \left\{ 2ba_2 \partial_\mu \partial_\nu R^{(1)} + \square \left(\bar{h}_{\mu\nu} - \frac{\bar{h}}{2} \eta_{\mu\nu} \right) + \frac{b}{3} (R^{(1)} + \mathcal{G}^{(1)}) \eta_{\mu\nu} \right\}. \quad (2.37)$$

Using this with equation (2.25) in equation (2.24) gives

$$-\frac{1}{2} \square \left(\bar{h}_{\mu\nu} - \frac{\bar{h}}{2} \eta_{\mu\nu} \right) - (b+1) \left(a_2 \partial_\mu \partial_\nu R^{(1)} + \frac{R^{(1)}}{6} \eta_{\mu\nu} \right) = \mathcal{G}^{(1)}_{\mu\nu} + \frac{b-2}{6} \mathcal{G}^{(1)} \eta_{\mu\nu}. \quad (2.38)$$

Picking $b = -1$ the second term vanishes, thus we will set^[31,33]

$$\bar{h}_{\mu\nu} = h_{\mu\nu} - \left(a_2 R^{(1)} + \frac{h}{2} \right) \eta_{\mu\nu} \quad (2.39)$$

$$h_{\mu\nu} = \bar{h}_{\mu\nu} - \left(a_2 R^{(1)} - \frac{\bar{h}}{2} \right) \eta_{\mu\nu}. \quad (2.40)$$

From equation (2.21) the Ricci scalar in this case is

$$\begin{aligned} R^{(1)} &= \square \left(a_2 R^{(1)} - \frac{\bar{h}}{2} \right) - \square(-4a_2 R^{(1)} - \bar{h}) \\ &= 3a_2 \square R^{(1)} + \frac{1}{2} \square \bar{h}. \end{aligned} \quad (2.41)$$

For consistency with equation (2.25), we require

$$-\frac{1}{2} \square \bar{h} = \mathcal{G}^{(1)}. \quad (2.42)$$

Inserting this into equation (2.38), with $b = -1$, we see

$$-\frac{1}{2} \square \bar{h}_{\mu\nu} = \mathcal{G}^{(1)}_{\mu\nu}; \quad (2.43)$$

we have our wave equation.

Should a_2 be sufficiently small that it may be regarded an $\mathcal{O}(\varepsilon)$ quantity, we recover GR to leading order within our analysis.

2.3 Gravitational Radiation

Having established two wave equations, (2.25) and (2.43), we may now investigate their solutions. We shall consider waves in a vacuum such that $\mathcal{G}_{\mu\nu} = 0$. Using a standard Fourier decomposition

$$\bar{h}_{\mu\nu} = \hat{h}_{\mu\nu}(k_\rho) \exp(ik_\rho x^\rho), \quad (2.44)$$

$$R^{(1)} = \hat{R}(q_\rho) \exp(iq_\rho x^\rho), \quad (2.45)$$

where k_μ and q_μ are 4-wavevectors. From equation (2.43) we know that k_μ is a null vector, so for a wave travelling along the z -axis

$$k^\mu = \frac{\omega}{c}(1, 0, 0, 1), \quad (2.46)$$

where ω is the angular frequency. Similarly, from equation (2.25)

$$q^\mu = \left(\frac{\Omega}{c}, 0, 0, \sqrt{\frac{\Omega^2}{c^2} - \mathcal{R}^2} \right), \quad (2.47)$$

for frequency Ω . These waves do not travel at c , but have a group velocity

$$v = \frac{c\sqrt{\Omega^2 - c^2\mathcal{R}^2}}{\Omega}, \quad (2.48)$$

provided that $\mathcal{R}^2 > 0$, $v < c$. For $\Omega < \Omega_R = c\mathcal{R}$, we will find an evanescently decaying wave instead of a propagating mode.

From the condition (2.35) we find that k^μ is orthogonal to $\hat{h}_{\mu\nu}$,

$$k^\mu \hat{h}_{\mu\nu} = 0, \quad (2.49)$$

thus in this case

$$\hat{h}_{0\nu} + \hat{h}_{3\nu} = 0. \quad (2.50)$$

Let us now consider the implications of equation (2.42) using equations (2.33) and (2.25),

$$\begin{aligned} \square(4a_2 R^{(1)} + h) &= 0 \\ \square h &= -\frac{4}{3}R^{(1)}. \end{aligned} \quad (2.51)$$

For non-zero $R^{(1)}$ (as required for the Ricci mode) there is no way we can make a gauge choice such that the trace h will vanish^[31, 33]. This is distinct from in GR. It is possible, however, to make a gauge choice such that the trace \bar{h} will vanish. Consider a gauge transformation generated by ξ_μ which satisfies $\square\xi_\mu = 0$, and so has a Fourier decomposition

$$\xi_\mu = \hat{\xi}_\mu \exp(ik_\rho x^\rho). \quad (2.52)$$

A transformation

$$\bar{h}_{\mu\nu} \rightarrow \bar{h}_{\mu\nu} + \partial_\mu \xi_\nu + \partial_\nu \xi_\mu - \eta_{\mu\nu} \partial^\rho \xi_\rho, \quad (2.53)$$

would ensure both conditions (2.35) and (2.43) are satisfied^[1]. Under such a transformation

$$\hat{\bar{h}}_{\mu\nu} \rightarrow \hat{\bar{h}}_{\mu\nu} + i \left(k_\mu \hat{\xi}_\nu + k_\nu \hat{\xi}_\mu - \eta_{\mu\nu} k^\rho \hat{\xi}_\rho \right). \quad (2.54)$$

We may therefore impose four further constraints (one for each $\hat{\xi}_\mu$) upon $\hat{\bar{h}}_{\mu\nu}$. We take these to be

$$\hat{\bar{h}}_{0\nu} = 0, \quad \hat{\bar{h}} = 0. \quad (2.55)$$

This may appear to be five constraints, however we have already imposed (2.50), and so setting $\hat{\bar{h}}_{00} = 0$ automatically implies $\hat{\bar{h}}_{03} = 0$. In this gauge we have

$$h_{\mu\nu} = \bar{h}_{\mu\nu} - a_2 R^{(1)} \eta_{\mu\nu}, \quad (2.56)$$

$$h = -4a_2 R^{(1)}. \quad (2.57)$$

Thus $\bar{h}_{\mu\nu}$ behaves just as its GR counterpart so we may define

$$[\hat{\bar{h}}_{\mu\nu}] = \begin{bmatrix} 0 & 0 & 0 & 0 \\ 0 & h_+ & h_\times & 0 \\ 0 & h_\times & -h_+ & 0 \\ 0 & 0 & 0 & 0 \end{bmatrix}, \quad (2.58)$$

where h_+ and h_\times are constants representing the amplitudes of the two transverse polarizations of gravitational radiation.

It is important that our solutions reduce to those of GR in the event that $f(R) = R$. In this linearized approach this corresponds to $a_2 \rightarrow 0$, $\Upsilon^2 \rightarrow \infty$. We see from equation (2.47) that in this limit it would take an infinite frequency to excite a propagating Ricci mode, and evanescent waves would decay away infinitely quickly. Therefore there would be no detectable Ricci modes and we would only observe the two polarizations found in GR. Additionally $\bar{h}_{\mu\nu}$ would simplify to its usual trace-reversed form.

2.4 $f(R)$ With A Source

Having considered radiation in a vacuum, we now move on to the case with a source term. We want a first order perturbation from our background metric so the linearized field equation is

$$\mathcal{G}^{(1)}_{\mu\nu} = \frac{8\pi G}{c^4} T_{\mu\nu}. \quad (2.59)$$

We will again assume a Minkowski background, considering terms to $\mathcal{O}(\varepsilon)$ only. To solve the wave equations (2.25) and (2.43) with this source term we use a Green's function

$$(\square + \Upsilon^2) \mathcal{G}_T(x, x') = \delta(x - x'), \quad (2.60)$$

where \square acts on x . The Green's function is familiar as the Klein-Gordon propagator (up to a factor of $-i$)^[34]

$$\mathcal{G}_\Upsilon(x, x') = \int \frac{d^4p}{(2\pi)^4} \frac{\exp[-ip \cdot (x - x')]}{\Upsilon^2 - p^2}. \quad (2.61)$$

This may be evaluated by a suitable contour integral to give

$$\mathcal{G}_\Upsilon(x, x') = \begin{cases} \int \frac{d\omega}{2\pi c} \exp[-i\omega(t - t')] \frac{1}{4\pi r} \exp\left[i\left(\frac{\omega^2}{c^2} - \Upsilon^2\right)^{1/2} r\right] & \omega^2 > \Omega_R^2 \\ \int \frac{d\omega}{2\pi c} \exp[-i\omega(t - t')] \frac{1}{4\pi r} \exp\left[-\left(\Upsilon^2 - \frac{\omega^2}{c^2}\right)^{1/2} r\right] & \omega^2 < \Omega_R^2 \end{cases}, \quad (2.62)$$

where we have introduced $ct = x^0$, $ct' = x'^0$ and $r = |\mathbf{x} - \mathbf{x}'|$. For $\Upsilon = 0$

$$\mathcal{G}_0(x, x') = \frac{\delta(ct - ct' - r)}{4\pi cr}, \quad (2.63)$$

the standard retarded-time Green's function. We can use this to solve equation (2.43)

$$\begin{aligned} \bar{h}_{\mu\nu}(x) &= -\frac{16\pi G}{c^4} \int d^4x' \mathcal{G}_0(x, x') T_{\mu\nu}(x') \\ &= -\frac{4G}{c^4} \int d^3x' \frac{T_{\mu\nu}(ct - r, \mathbf{x}')}{r}. \end{aligned} \quad (2.64)$$

This is exactly as in GR, so we may use standard results.

Solving for the scalar mode

$$R^{(1)}(x) = -\frac{8\pi G\Upsilon^2}{c^4} \int d^4x' \mathcal{G}_\Upsilon(x, x') T(x'). \quad (2.65)$$

To proceed further we must know the form of the trace $T(x')$. In general the form of $R^{(1)}(x)$ will be complicated.

2.4.1 The Newtonian Limit

Let us consider the limiting case of a Newtonian source, such that

$$T_{00} = c^2\rho; \quad |T_{00}| \gg |T_{0i}|; \quad |T_{00}| \gg |T_{ij}|, \quad (2.66)$$

with a mass distribution of a stationary point source

$$\rho = M\delta(\mathbf{x}'). \quad (2.67)$$

This source does not produce any radiation. As in GR we find

$$\bar{h}_{00} = -\frac{4GM}{c^2 r}; \quad \bar{h}_{0i} = \bar{h}_{ij} = 0. \quad (2.68)$$

Solving for the Ricci scalar term gives

$$R^{(1)} = -\frac{2G\Upsilon^2 M \exp(-\Upsilon r)}{c^2 r}. \quad (2.69)$$

Combining these in equation (2.40) yields a metric perturbation with non-zero elements

$$h_{00} = -\frac{2GM}{c^2 r} \left[1 + \frac{\exp(-\Upsilon r)}{3} \right]; \quad h_{ii} = -\frac{2GM}{c^2 r} \left[1 - \frac{\exp(-\Upsilon r)}{3} \right] \quad (\text{no sum}). \quad (2.70)$$

Thus, to first order, the metric for a point mass in $f(R)$ -gravity is^[35, 36]

$$\begin{aligned} ds^2 = & \left\{ 1 - \frac{2GM}{c^2 r} \left[1 + \frac{\exp(-\Upsilon r)}{3} \right] \right\} c^2 dt^2 \\ & - \left\{ 1 + \frac{2GM}{c^2 r} \left[1 - \frac{\exp(-\Upsilon r)}{3} \right] \right\} (dx^2 + dy^2 + dz^2). \end{aligned} \quad (2.71)$$

This is not the linearized limit of the Schwarzschild metric, although it is recovered as $a_2 \rightarrow 0$, $\Upsilon \rightarrow \infty$. Therefore the Schwarzschild solution is not a black hole (BH) solution in $f(R)$ -gravity^[37]. This metric has already been derived for the case of quadratic gravity, which includes terms like R^2 and $R_{\mu\nu}R^{\mu\nu}$ in the Lagrangian^[28, 29, 38, 39]. In linearized theory our $f(R)$ reduces to quadratic theory, as to first order $f(R) = R + a_2 R^2$.

We may extend this result to a slowly rotating source with angular momentum J ; then we have the additional term^[32]

$$\bar{h}^{0i} = -\frac{2G}{c^2 r^3} \epsilon^{ijk} J_j x_k, \quad (2.72)$$

where ϵ^{ijk} is the alternating Levi-Civita tensor. The metric is

$$\begin{aligned} ds^2 = & \left\{ 1 - \frac{2GM}{c^2 r} \left[1 + \frac{\exp(-\Upsilon r)}{3} \right] \right\} c^2 dt^2 + \frac{4GJ}{c^2 r^3} (x dy - y dx) dt \\ & - \left\{ 1 + \frac{2GM}{c^2 r} \left[1 - \frac{\exp(-\Upsilon r)}{3} \right] \right\} (dx^2 + dy^2 + dz^2), \end{aligned} \quad (2.73)$$

where z is the rotation axis. This is not the first order limit of the Kerr metric, aside from in the limit $a_2 \rightarrow 0$, $\Upsilon \rightarrow \infty$.

It has been suggested that since $R = 0$ is a valid solution to the vacuum equations, the BH solutions of GR should also be solutions in $f(R)$ ^[9, 40]. However we see here that this is not the case: to have a BH you must have a source, and, because of equation (2.25), this forces R to be non-zero in the surrounding vacuum, although it will decay to zero at infinity^[41]. It should therefore be possible to distinguish between theories by observing the BHs that form.

Solving the full field equations to find the exact BH metric in $f(R)$ is difficult because of the higher-order derivatives that enter the equations. Any solution must have the appropriate limiting form as given above.

In $f(R)$ -gravity Birkhoff's theorem no longer applies: the metric about a spherically symmetric mass does not correspond to the equivalent of the Schwarzschild solution, since the distribution of matter influences how the Ricci scalar decays, and consequently

Gauss' theorem no longer applies. Repeating our analysis for a (non-rotating) sphere of uniform density and radius L we find

$$\bar{h}_{00} = -\frac{4GM}{c^2 r}; \quad \bar{h}_{0i} = \bar{h}_{ij} = 0, \quad (2.74)$$

as in GR, and for the point mass, but

$$R^{(1)} = -\frac{6GM \exp(-\Upsilon r)}{c^2} \frac{1}{r} \left[\frac{\Upsilon L \cosh(\Upsilon L) - \sinh(\Upsilon L)}{\Upsilon L^3} \right] \quad (2.75)$$

$$= -\frac{6GM \exp(-\Upsilon r)}{c^2} \frac{1}{r} \Upsilon^2 \Xi(\Upsilon L), \quad (2.76)$$

defining $\Xi(\Upsilon L)$ in the last line.³ The metric perturbation thus has non-zero first order elements^[39, 42]

$$h_{00} = -\frac{2GM}{c^2 r} [1 + \exp(-\Upsilon r) \Xi(\Upsilon L)]; \quad h_{ii} = -\frac{2GM}{c^2 r} [1 - \exp(-\Upsilon r) \Xi(\Upsilon L)] \quad (\text{no sum}). \quad (2.77)$$

where we have assumed that $r > L$ at all stages.⁴

2.4.2 Fifth-Force Tests

From the metric equation (2.71) we see that a point mass has a Yukawa gravitational potential^[35, 39]

$$U(r) = \frac{GM}{r} \left[1 + \frac{\exp(-\Upsilon r)}{3} \right]. \quad (2.78)$$

Potentials of this form are well studied in fifth-force tests^[2, 43, 44] which consider a potential defined by a coupling constant α and a length-scale λ such that

$$U(r) = \frac{GM}{r} \left[1 + \alpha \exp\left(-\frac{r}{\lambda}\right) \right]. \quad (2.79)$$

We are able to put strict constraints upon our length-scale λ_R , and hence a_2 , since our coupling constant $\alpha_R = 1/3$ is relatively large. We would expect this coupling constant to be larger for extended sources: comparison with equation (2.77) shows that for a uniform sphere $\alpha_R = \Xi(\Upsilon L) \geq 1/3$.

The best constraints at short distances come from the Eöt-Wash experiments, which use torsion balances^[45, 46]. These constrain $\lambda_R \lesssim 8 \times 10^{-5} \text{ m}$. Hence we determine $|a_2| \lesssim 2 \times 10^{-9} \text{ m}^2$. A similar result is obtained by Näf and Jetzer^[36]. This would mean that the cut-off frequency for a propagating scalar mode would be $\Omega_R \gtrsim 4 \times 10^{12} \text{ s}^{-1}$. This is much higher than expected for astrophysical objects.

Fifth-force tests also permit λ_R to be large. This degeneracy can be broken using other tests. From equation (2.71), calculating the post-Newtonian parameter γ , which measures the space-curvature produced by unit rest mass^[2], we find^[12, 41]

$$\gamma = \frac{3 - \exp(-\Upsilon r)}{3 + \exp(-\Upsilon r)}. \quad (2.80)$$

³ $\Xi(0) = 1/3$ is the minimum of $\Xi(\Upsilon L)$.

⁴ Inside the source $R^{(1)} = -6GM [1 - (\Upsilon L + 1) \exp(-\Upsilon L) \sinh(\Upsilon r) / \Upsilon r] / c^2 L^3$.

As $\Upsilon \rightarrow \infty$, the GR value of $\gamma = 1$ is recovered. To be consistent with the current observational values of $\gamma = 1 + (2.1 \pm 2.3) \times 10^{-5}$ [2, 47] we must require $\Upsilon r \gg 1$ on solar system scales. This excludes the larger range for λ_R . Note that this bound for γ was derived assuming that it was independent of position. We will see that the large range for λ_R is also excluded by planetary perihelion precession in section 2.4.4.

While the laboratory bound on λ_R may be strict compared to astronomical length-scales, it is still much greater than the expected characteristic gravitational scale, the Planck length ℓ_P . We might expect for a natural quantum theory, that $a_2 \sim \mathcal{O}(\ell_P^2)$; however $\ell_P^2 = 2.612 \times 10^{-70} \text{ m}^2$, thus the bound is still about 60 orders of magnitude greater than the natural value. The only other length-scale that we could introduce would be defined by the cosmological constant Λ . Using the concordance values [48] $\Lambda = 1.27 \times 10^{-52} \text{ m}^{-2}$; we see that $\Lambda^{-1} \gg |a_2|$. It is intriguing to note that if we combine these two length-scales we find $\ell_P/\Lambda^{1/2} = 1.44 \times 10^{-9} \text{ m}^2$, which is on the order of the current bound. This is likely to be a coincidence, since there is nothing fundamental about the level of current precision. It would be interesting to see if the measurements could be improved to rule out a Yukawa interaction around this length-scale.

Here we have only discussed tests in the solar system. It may be, if $f(R)$ is just an effective theory, that the value of a_2 is different in different regions. This may allow the Ricci mode to be excited and propagate outside of the solar system. We discuss this more in section 2.5.

2.4.3 The Weak-Field Metric

To continue working with the weak-field metric, equation (2.71), it is useful to transform it to the more familiar form

$$ds^2 = A(\tilde{r})c^2 dt^2 - B(\tilde{r})d\tilde{r}^2 - \tilde{r}^2 d\Omega^2. \quad (2.81)$$

The coordinate \tilde{r} is a circumferential measure, as in the Schwarzschild metric, as opposed to r , used in preceding sections, which is a radial distance, an isotropic coordinate [1, 41]. To simplify the algebra we shall introduce the Schwarzschild radius

$$r_S = \frac{2GM}{c^2}. \quad (2.82)$$

In the linearized regime, we require that the new radial coordinate satisfies

$$\tilde{r}^2 = \left\{ 1 + \frac{r_S}{r} \left[1 - \frac{\exp(-\Upsilon r)}{3} \right] \right\} r^2 \quad (2.83)$$

$$\tilde{r} = r + \frac{r_S}{2} \left[1 - \frac{\exp(-\Upsilon r)}{3} \right]. \quad (2.84)$$

To first order in r_S/r [41]

$$A(\tilde{r}) = 1 - \frac{r_S}{\tilde{r}} \left[1 + \frac{\exp(-\Upsilon r)}{3} \right]. \quad (2.85)$$

We see that the functional form of g_{00} is almost unchanged upon substituting \tilde{r} for r ; however r is still in the exponential.

To find $B(\tilde{r})$ we consider, using equation (2.84),

$$\begin{aligned} \frac{d\tilde{r}}{\tilde{r}} &= d \ln \tilde{r} \\ &= \left\{ \frac{1 + \Upsilon r_S r \exp(-\Upsilon r)/6\tilde{r}}{1 + (r_S/2\tilde{r})[1 - \exp(-\Upsilon\tilde{r})/3]} \right\} \frac{dr}{\tilde{r}}. \end{aligned} \quad (2.86)$$

Thus

$$d\tilde{r}^2 = \frac{\tilde{r}^2}{r^2} \left\{ \frac{1 + \Upsilon r_S r \exp(-\Upsilon r)/6\tilde{r}}{1 + (r_S/2\tilde{r})[1 - \exp(-\Upsilon\tilde{r})/3]} \right\} dr^2. \quad (2.87)$$

The term in braces is $[B(\tilde{r})]^{-1}$. To proceed further we must check the size of $\Upsilon r_S \exp(-\Upsilon r)$. We assume that in the weak-field

$$\varepsilon = \frac{r_S}{r} \quad (2.88)$$

is small. Then the metric perturbations from Minkowski are small. Now

$$\begin{aligned} \Upsilon r_S \exp(-\Upsilon r) &= r\varepsilon\Upsilon \exp(-\Upsilon r) \\ &= \varepsilon\chi \exp(-\chi), \end{aligned} \quad (2.89)$$

defining $\chi = \Upsilon r$. The function $\chi \exp(-\chi)$ has a maximum value when $\chi = 1$, hence

$$\Upsilon r_S \exp(-\Upsilon r) \leq \varepsilon \exp(-1). \quad (2.90)$$

This term is also $\mathcal{O}(\varepsilon)$. Expanding to first order^[41]

$$B(\tilde{r}) = 1 + \frac{r_S}{\tilde{r}} \left[1 + \frac{\exp(-\Upsilon r)}{3} \right] - \frac{\Upsilon r_S \exp(-\Upsilon r_S)}{3}. \quad (2.91)$$

In the limit $\Upsilon \rightarrow \infty$, where we recover GR, $A(\tilde{r})$ and $B(\tilde{r})$ tend to their Schwarzschild forms.

2.4.4 Epicyclic Frequencies

One means of probing the nature of a spacetime is through observations of orbital motions^[49]. We will consider the epicyclic motion produced by perturbing a circular orbit. We will start by deriving a general result for any metric of the form of equation (2.81), and then use this for our $f(R)$ solution. For this section we shall adopt units with $c = 1$.

For any metric of the form of equation (2.81) there are three constants of motion: the orbiting particle's rest mass μ , the energy (per unit mass) of the orbit E , and the z -component of the angular momentum (per unit mass) L . Using an over-dot to denote differentiation with respect to an affine parameter, which we shall identify as proper time τ ,

$$E = A\dot{t}; \quad (2.92)$$

$$L = \tilde{r}^2 \sin^2 \theta \dot{\phi}. \quad (2.93)$$

As a consequence of the spherical symmetry we may confine the motion to the equatorial plane $\theta = \pi/2$ without loss of generality. From the Hamiltonian $\mathcal{H} = g_{\mu\nu}\dot{x}^\mu\dot{x}^\nu$ we obtain the equation of motion for massive particles

$$\dot{\tilde{r}}^2 = \frac{E^2}{AB} - \frac{1}{B} \left(1 + \frac{L^2}{\tilde{r}^2} \right). \quad (2.94)$$

Hence for a circular orbit

$$E^2 = A \left(1 + \frac{L^2}{\tilde{r}^2} \right). \quad (2.95)$$

Differentiating equation (2.94) yields

$$\ddot{\tilde{r}} = -\frac{E^2}{2AB} \left(\frac{A'}{A} + \frac{B'}{B} \right) + \frac{B'}{2B^2} \left(1 + \frac{L^2}{\tilde{r}^2} \right) + \frac{L^2}{\tilde{r}^3 B}, \quad (2.96)$$

where a prime signifies differentiation with respect to \tilde{r} . For a circular orbit

$$0 = \frac{2L^2}{\tilde{r}^3} - \frac{A'}{A} \left(1 + \frac{L^2}{\tilde{r}^2} \right). \quad (2.97)$$

Thus a circular orbit is defined by one of $\{E, L, \tilde{r}\}$. We will consider a small perturbation to a circular orbit. Perturbations out of the plane just redefine the orbital plane; they are not of interest. A radial perturbation may be parameterized as

$$\tilde{r} = \bar{r} + \delta, \quad (2.98)$$

where \bar{r} is the radius of the unperturbed orbit. We will denote $A(\bar{r}) = \bar{A}$ and $B(\bar{r}) = \bar{B}$. Substituting into equation (2.96) and retaining terms to first order

$$\ddot{\delta} = -\frac{2\bar{A}^2 L^2}{\bar{r}^3 \bar{A}' \bar{B}} \left(\frac{\bar{A}''}{2\bar{A}^2} - \frac{\bar{A}'^2}{\bar{A}^3} \right) \delta + \frac{3L^2}{\bar{r}^4} \delta. \quad (2.99)$$

Assuming a solution of form $\delta = \delta_0 \cos(-i\Omega\tau)$,

$$\Omega^2 = \frac{L^2}{\bar{r}^3 \bar{B}} \left(\frac{\bar{A}''}{\bar{A}'} - \frac{2\bar{A}'}{\bar{A}} + \frac{3}{\bar{r}} \right). \quad (2.100)$$

We may rewrite the radial motion as

$$\tilde{r} = \bar{r} + \delta_0 \cos(-i\Omega\tau). \quad (2.101)$$

If we compare this with an elliptic Keplerian orbit of small eccentricity e

$$\tilde{r} = \frac{a(1 - e^2)}{1 + e \cos(\omega_0\tau)} \quad (2.102)$$

$$= a [1 - e \cos(\omega_0\tau) + \dots] \quad (2.103)$$

to first order in e , where a is the semimajor axis and ω_0 is the orbital frequency; we may identify our perturbed orbit with an elliptical orbit where^[50]

$$\bar{r} = a; \quad \delta_0 = -ea. \quad (2.104)$$

The eccentricity is the small parameter $|e| = |\delta_0/r| \ll 1$. To this accuracy one cannot distinguish between a and the semilatus rectum $p = a(1 - e^2)$.

Unless $\omega_0 = \Omega$ the elliptical motion will be asynchronous with the orbital motion: there will be precession of the periapsis. The orbital frequency is

$$\omega_0^2 = \frac{L^2}{\bar{r}^4}. \quad (2.105)$$

In one revolution the ellipse will precess about the focus by

$$\begin{aligned} \varpi &= \omega_0 \left(\frac{2\pi}{\Omega} - \frac{2\pi}{\omega_0} \right) \\ &= 2\pi \left(\frac{\omega_0}{\Omega} - 1 \right) \end{aligned} \quad (2.106)$$

The precession is cumulative, so a small deviation may be measurable over sufficient time.

For the $f(R)$ metric defined by equations (2.85) and (2.91) the epicyclic frequency is

$$\Omega^2 = \omega_0^2 \left[1 - \frac{3r_S}{\bar{r}} - \zeta(\Upsilon, r_S, \bar{r}) \right], \quad (2.107)$$

defining the function

$$\begin{aligned} \zeta(\Upsilon, r_S, \bar{r}) &= r_S \left(\frac{1}{3\bar{r}} + \Upsilon \right) \exp(-\Upsilon \bar{r}) + \frac{\Upsilon^2 \bar{r}^2 \exp(-\Upsilon \bar{r})}{3 + (1 + \Upsilon \bar{r}) \exp(-\Upsilon \bar{r})} \\ &\times \left\{ 1 - \frac{r_S}{\bar{r}} \left[1 + \frac{\exp(-\Upsilon \bar{r})}{3} \right] - \frac{\Upsilon r_S \exp(-\Upsilon \bar{r})}{3} \right\}. \end{aligned} \quad (2.108)$$

This characterizes the deviation from the Schwarzschild case: the change in the precession per orbit relative to Schwarzschild is

$$\Delta\varpi = \varpi - \varpi_S \quad (2.109)$$

$$= \pi\zeta, \quad (2.110)$$

using the subscript S to denote the Schwarzschild value. To obtain the last line we have expanded to lowest order, assuming that ζ is small.⁵ Since $\zeta \geq 0$, the precession rate is enhanced relative to GR.

Let us now apply this to the classic test of planetary precession in the solar system. Table 2.1 shows the orbital properties of the planets. We will use the deviation in perihelion precession rate from the GR prediction to constrain the value of ζ , and hence Υ and a_2 . Since several of the deviations are negative, they cannot be explained by

⁵There is one term in ζ that is not explicitly $\mathcal{O}(\varepsilon)$. Numerical evaluation shows that this is < 0.6 for the applicable range of parameters.

Planet	Semimajor axis ^[51] $r/10^{11}$ m	Orbital period ^[51] $(2\pi/\omega_0)/\text{yr}$	Precession rate ^[52] $\Delta\varpi \pm \sigma_{\Delta\varpi}/\text{mas yr}^{-1}$	Eccentricity ^[51] e
Mercury	0.57909175	0.24084445	-0.040 ± 0.050	0.20563069
Venus	1.0820893	0.61518257	0.24 ± 0.33	0.00677323
Earth	1.4959789	0.99997862	0.06 ± 0.07	0.01671022
Mars	2.2793664	1.88071105	-0.07 ± 0.07	0.09341233
Jupiter	7.7841202	11.85652502	0.67 ± 0.93	0.04839266
Saturn	14.267254	29.42351935	-0.10 ± 0.15	0.05415060
Uranus	28.709722	83.74740682	-38.9 ± 39.0	0.04716771
Neptune	44.982529	163.723204	-44.4 ± 54.0	0.00858587
Pluto	59.063762	248.0208	28.4 ± 25.1	0.24880766

Table 2.1: Orbital properties of the eight major planets and Pluto. We take the semimajor orbital axis to be the flat-space distance r , not the coordinate \tilde{r} . The eccentricity is not used in calculations, but is given to assess the accuracy of neglecting terms $\mathcal{O}(e^2)$.

$f(R)$ corrections. This may be considered as evidence against $f(R)$ -gravity; however, all the precession rates are consistent with GR predictions ($\Delta\varpi = 0$), thus we cannot conclusively rule out $f(R)$ -gravity. Since the deviations are zero to within their uncertainties, we may use the size of these uncertainties to constrain the $f(R)$ correction. Table 2.2 shows the constraints for Υ and a_2 obtained by equating the uncertainty in the precession rate $\sigma_{\Delta\varpi}$ with the $f(R)$ correction, and similarly using twice the uncertainty $2\sigma_{\Delta\varpi}$.

Planet	Using $\sigma_{\Delta\varpi}$		Using $2\sigma_{\Delta\varpi}$	
	$\Upsilon/10^{-11} \text{ m}^{-1}$	$ a_2 /10^{18} \text{ m}^2$	$\Upsilon/10^{-11} \text{ m}^{-1}$	$ a_2 /10^{18} \text{ m}^2$
Mercury	52.6	1.2	51.3	1.3
Venus	25.3	5.2	24.6	5.5
Earth	19.1	9.1	18.6	9.6
Mars	12.2	22	11.9	24
Jupiter	2.96	380	2.87	410
Saturn	1.69	1200	1.63	1200
Uranus	0.58	9800	0.56	11000
Neptune	0.35	28000	0.33	31000
Pluto	0.26	49000	0.25	55000

Table 2.2: Bounds calculated using uncertainties in planetary perihelion precession rates. Υ must be greater than or equal to the tabulated value, $|a_2|$ must be less than or equal to the tabulated value.

While the presence of negative deviations is evidence against $f(R)$ -gravity, the tightest numerical constraint, obtained from the orbit of Mercury, is many orders of magnitude worse than obtained from laboratory tests in section 2.4.2. This bound is not much more stringent than the requirement that $\Upsilon r > 1$ over solar system scales. This is not surprising: for there to be a measurable precession effect the $f(R)$ modification to gravity must be significant; this implies that $\exp(-\Upsilon r)$ cannot be negligibly small.

2.5 Discussion & Remaining Questions

We have seen that gravitational radiation is modified in $f(R)$ -gravity, as the Ricci scalar is no longer constrained to be zero. In linearized theory we find that there is an additional mode of oscillation, that of the Ricci scalar. However, based upon constraints from fifth-force experiments this mode seems unlikely to be excited in astrophysical processes. In $f(R)$ theory, the two transverse GW modes are modified from their GR counterparts to include a contribution from the Ricci scalar, see equation (2.40), allowing us to probe the curvature of the strong-field regions from which GWs originate. However, further study is needed in order to understand how GW waves behave in a region with background curvature, in particular when R is non-zero. This will be done in subsequent work.

Gravitational radiation is not the only way to test $f(R)$ theory. From linearized theory we have deduced the weak-field metrics for some simple mass distributions. These indicate that BH solutions are not the same as in GR. Using these weak-field results it is possible to constrain some parameters of $f(R)$. The strongest constraints come from fifth-force tests, but we have also derived the epicyclic frequency for near circular orbits. This is as an independent measurement, perhaps to check $f(R)$ in a different regime. We find that the current errors in planetary precession rates are too large to be explained by $f(R)$ modifications; they require a_2 to be unreasonably large. Additionally, some of the estimated deviations from GR precession rates are negative, which cannot be achieved with $f(R)$ corrections. Since all of the deviations are consistent with zero, we cannot use these as proof against $f(R)$, just that it does not modify gravity on solar system scales.

It is possible that $f(R)$ -gravity is not universal — that it is different in different regions of space. This could occur if $f(R)$ is just an approximate effective theory, then the range of a particular parametrization's applicability could be limited to a specific domain. For example, we could imagine that the effective theory in the vicinity of a massive BH where the curvature is large is different from in the solar system where curvature is small; alternatively $f(R)$ could evolve with cosmological epoch so that it varies with redshift.

Another possibility is that $f(R)$ -gravity is modified in the presence of matter via the chameleon mechanism^[53, 54]. In metric $f(R)$ this corresponds to a nonlinear effect arising from a large departure of the Ricci scalar from its background value^[12]. The mass of the effective scalar degree of freedom then depends upon the density of its environment. In a region of high matter density, such as the Earth, the deviations from standard gravity would be exponentially suppressed due to a large effective \mathcal{V} ; while on cosmological scales, where the density is low, the scalar would have a small \mathcal{V} , perhaps of the order H_0/c ^[53, 54]. The chameleon mechanism allows $f(R)$ gravity to pass solar system tests while remaining of interest for cosmology. In the context of gravitational radiation, this would mean that the Ricci scalar mode could freely propagate on cosmological scales^[55]. Unfortunately, since the chameleon mechanism suppresses the effects of $f(R)$ in the presence of matter, this mode would have to be excited by something other than the movement of matter.

An obvious extension to the work presented here is to consider the case when a_0 is non-zero. We could then consider an expansion about (anti-)de Sitter space. This is interesting because the current Λ CDM paradigm indicates that we live in a universe

with a positive cosmological constant^[48].

Chapter 3

Parabolic Encounters Of A Massive Black Hole

3.1 Background & Introduction

Currently it is understood that many, if not all, galactic nuclei harboured a black hole at some point^[56, 57]. The best opportunity to study these objects comes from the compact object in our own galactic centre (GC), which is coincident with Sagittarius A* (Sgr A*). This is identified as a massive black hole (MBH) of mass $M_{\bullet} = 4.31 \times 10^6 M_{\odot}$ at a distance of only $R_0 = 8.33 \text{ kpc}$ ^[58]. According to the no-hair theorem the MBH should be described completely by its mass M_{\bullet} and spin a (since we expect the charge of an astrophysical black hole to be negligible)^[59–64]. Consequently, measuring the spin is necessary to fully understand the MBH and its role in the evolution of the Galaxy. It has been suggested that the spin could be inferred from careful observation of the orbits of stars within a few milliparsecs of the GC^[65], although this is complicated because of perturbations due to other stars, or from observations of quasi-periodic oscillations (QPOs) of radio emissions^[66], though there are difficulties in interpreting these results^[9].

An exciting means of inferring information about the MBH is through gravitational waves (GWs) emitted when compact objects (COs), such as smaller BHs, neutron stars (NSs), white dwarfs (WDs) or low mass main sequence (MS) stars, pass close by. The planned LISA mission is designed to be able to detect GWs in the frequency range of interest for these encounters^[7, 8]. The identification of waves requires a set of accurate waveform templates covering parameter space. Much work has already been done on the waveforms generated when companion objects inspiral towards an MBH; as they orbit, the GWs carry away energy and angular momentum, causing the orbit to shrink until eventually the object plunges into the MBH. The initial orbits may be highly elliptical and a burst of radiation is emitted during each close encounter. These are known as extreme mass-ratio bursts (EMRBs)^[67]. Assuming that the companion is not scattered from its orbit, and does not plunge straight into the MBH, its orbit will evolve, becoming more circular, and it will begin to emit continuously significant gravitational radiation in the LISA frequency range. The resulting signals are known as extreme mass-ratio inspirals (EMRIs).

Studies of these systems have usually focused upon when the orbit completes multiple cycles, thus allowing a high signal-to-noise ratio to be accumulated. Here, we will investigate what can be learnt from high eccentricity orbits. These are the initial orbits onto which we expect that COs may be scattered by interactions with other bodies. The event rate for the detection of such EMRBs with LISA has been estimated to be as high as 15 yr^{-1} [67], although this has been revised downwards to the order of 1 yr^{-1} [68]. Even if only a single burst is detected during the LISA mission, this is still an exciting possibility since the information carried by the GW should give an unparalleled probe of the structure of spacetime of the GC. Exactly what can be inferred will depend upon the orbit.

We will make the simplifying assumption that all these orbits are marginally bound, or parabolic, since highly eccentric orbits will appear almost indistinguishable from an appropriate parabolic orbit [69]. Here “parabolic” and “eccentricity” refer to the energy of the geodesic and not to the geometric shape of the orbit.¹ Following such a trajectory an object may make just one pass of the MBH or, if the periapsis distance is small enough, it may complete a number of rotations. Such an orbit is referred to as zoom-whirl.

In order to compute the gravitational waveform produced in such a case, we integrate the geodesic equations for a parabolic orbit in Kerr spacetime. We assume that the orbiting body is a test particle, such that it does not influence the underlying spacetime, and that the orbital parameters evolve negligibly during the orbit so that they may be held constant. We use this to construct an approximate numerical kludge waveform [70].

3.2 Parabolic Orbits in Kerr Spacetime

3.2.1 The Metric & Geodesic Equations

Astrophysical BHs are described by the Kerr metric [71]. In standard Boyer-Lindquist coordinates the line element is [32, 72]

$$ds^2 = \frac{\rho^2 \Delta}{\Sigma^2} c^2 dt^2 - \frac{\Sigma \sin^2 \theta}{\rho^2} (d\phi - \omega dt)^2 - \frac{\rho^2}{\Delta} dr^2 - \rho^2 d\theta^2, \quad (3.1)$$

where we have introduced functions

$$\rho^2 = r^2 + a^2 \cos^2 \theta, \quad (3.2)$$

$$\Delta = r^2 - \frac{2GM_\bullet r}{c^2} + a^2, \quad (3.3)$$

$$\Sigma = (r^2 + a^2)^2 - a^2 \Delta \sin^2 \theta, \quad (3.4)$$

$$\omega = \frac{2GM_\bullet a r}{c \Sigma}. \quad (3.5)$$

The spin parameter is related to the BH’s angular momentum by

$$J = M_\bullet a c. \quad (3.6)$$

¹Marginally bound Keplerian orbits in flat spacetime are parabolic in both senses.

For the remainder of this section we shall work in natural units with $G = c = 1$.

Geodesics are parameterized by three conserved quantities (aside from the particle's mass μ): energy (per unit mass) E , specific angular momentum about the symmetry axis (the z -axis) L_z , and Carter constant Q ^[64, 73]. The geodesic equations are

$$\rho^2 \frac{dt}{d\tau} = a \left(L_z - aE \sin^2 \theta \right) + \frac{r^2 + a^2}{\Delta} T, \quad (3.7)$$

$$\rho^2 \frac{dr}{d\tau} = \pm \sqrt{V_r}, \quad (3.8)$$

$$\rho^2 \frac{d\theta}{d\tau} = \pm \sqrt{V_\theta}, \quad (3.9)$$

$$\rho^2 \frac{d\phi}{d\tau} = \frac{L_z}{\sin^2 \theta} - aE + \frac{a}{\Delta} T, \quad (3.10)$$

where we have introduced potentials

$$T = E \left(r^2 + a^2 \right) - aL_z, \quad (3.11)$$

$$V_r = T^2 - \Delta \left[r^2 + (L_z - aE)^2 + Q \right], \quad (3.12)$$

$$V_\theta = Q - \cos^2 \theta \left[a^2 \left(1 - E^2 \right) + \frac{L_z^2}{\sin^2 \theta} \right], \quad (3.13)$$

and τ is proper time. The signs of the r and θ equations may be chosen independently.

For a parabolic orbit $E = 1$, thus the particle is at rest at infinity. This simplifies the geodesic equations. It also allows us to give a simple interpretation for Carter constant Q : this is defined as

$$Q = L_\theta^2 + \cos^2 \theta \left[a^2 \left(1 - E^2 \right) + \frac{L_z^2}{\sin^2 \theta} \right], \quad (3.14)$$

where L_θ is the (non-conserved) specific angular momentum in the θ -direction (note $L_\theta^2 = V_\theta$). For $E = 1$ we have

$$\begin{aligned} Q &= L_\theta^2 + \cot^2 \theta L_z^2 \\ &= L_\infty^2 - L_z^2 \end{aligned} \quad (3.15)$$

where L_∞ is the total specific angular momentum at infinity, where the metric is asymptotically flat^[74].² This is as in Schwarzschild spacetime.

3.2.2 Integration Variables & Turning Points

In integrating the geodesic equations difficulties can arise because of the presence of turning points in the motion, when the sign of the r or θ geodesic equation will change.

²See Rosquist *et al.*^[75] for an interesting discussion of the interpretation of Q in the limit $G \rightarrow 0$ corresponding to a flat spacetime.

The radial turning points are at the periapsis r_p and at infinity. We may locate the periapsis by finding the roots of

$$V_r = 0$$

$$2M_\bullet r^3 - (L_z^2 + Q)r^2 + 2M_\bullet [(L_z - a)^2 + Q]r - a^2 Q = 0. \quad (3.16)$$

This has three roots, which we shall denote $\{r_1, r_2, r_p\}$; the periapsis r_p is the largest real root. We do not find the apoapsis as a (fourth) root to this equation as we have removed it by taking $E = 1$ before solving: it is simple to show this is a turning point by setting the unconstrained expression for V_r equal to zero, and then solving for $E(r)$; taking the limit $r \rightarrow \infty$ gives $E \rightarrow 1$ [76].

We may avoid the difficulties of the turning point by introducing an angular variable that always increases with proper time [77]: inspired by Keplerian orbits, we parameterize our trajectory by

$$r = \frac{p}{1 + e \cos \psi}, \quad (3.17)$$

where $e = 1$ is the eccentricity and $p = 2r_p$ is the semilatus rectum. As ψ covers its full range from $-\pi$ to π , r traces out one full orbit from infinity through the periapsis at $\psi = 0$ back to infinity. The geodesic equation for ψ is

$$\rho^2 \frac{d\psi}{d\tau} = \left\{ M_\bullet \left[2r_p - (r_1 + r_2)(1 + \cos \psi) + \frac{r_1 r_2}{2r_p} (1 + \cos \psi)^2 \right] \right\}^{1/2}. \quad (3.18)$$

This may be integrated without problem. Parameterizing an orbit by its periapsis and eccentricity has the additional benefit of allowing easier comparison with its flat-space equivalent [78].

The θ motion is usually bounded, with $\theta_0 \leq \theta \leq \pi - \theta_0$; in the event that $L_z = 0$ the particle follows a polar orbit and θ will cover its full range. The turning points are given by

$$V_\theta = 0$$

$$Q - \cot^2 \theta L_z^2 = 0. \quad (3.19)$$

Only if $L_z = 0$ may we reach the poles [76]. If we change variable to $\zeta = \cos^2 \theta$, we have a maximum value $\zeta_0 = \cos^2 \theta_0$ given by

$$\zeta_0 = \frac{Q}{Q + L_z^2} \quad (3.20)$$

$$= \frac{Q}{L_\infty^2}. \quad (3.21)$$

See figure 3.1 for a geometrical visualization. Let us now introduce a second angular variable [77]

$$\zeta = \zeta_0 \cos^2 \chi. \quad (3.22)$$

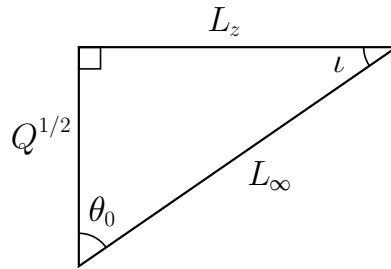


Figure 3.1: The angular momenta L_∞ , L_z and \sqrt{Q} define a right-angled triangle. The acute angles are θ_0 , the extremal value of the polar angle, and ι , the orbital inclination^[79].

Over one 2π period of χ , θ oscillates over its full range, from its minimum value to its maximum and back. The geodesic equation for χ is

$$\rho^2 \frac{d\chi}{d\tau} = \sqrt{Q + L_z^2}, \quad (3.23)$$

and may be integrated simply.

3.3 Waveform Construction

With the geodesic calculated for given angular momenta L_z and Q , and initial starting position, the orbiting body is assumed to follow this trajectory exactly: we ignore evolution due to the radiation of energy and angular momentum. From this we calculate the waveform using a semirelativistic approximation^[80]: we assume that the particle moves along a geodesic in the Kerr geometry, but radiates as if it were in flat spacetime. This quick-and-dirty technique is known as a numerical kludge (NK), and has been shown to approximate well results computed by more accurate methods^[70].

3.3.1 Kludge Approximation

Numerical kludge approximations aim to encapsulate the main characteristics of a waveform by using the exact particle trajectory (ignoring inaccuracies from the evolution of the orbital parameters), whilst saving on computational time by using approximate waveform generation techniques. To start, we build an equivalent flat-space trajectory from the Kerr geodesic. This is done by identifying the Boyer-Lindquist coordinates with a set of flat-space coordinates; we consider two choices here:

1. Identify the Boyer-Lindquist coordinates with flat-space spherical polars $\{r_{\text{BL}}, \theta_{\text{BL}}, \phi_{\text{BL}}\} \rightarrow \{r_{\text{sph}}, \theta_{\text{sph}}, \phi_{\text{sph}}\}$, then define flat-space Cartesian coordinates^[70, 78]

$$\mathbf{x} = (r_{\text{sph}} \sin \theta_{\text{sph}} \cos \phi_{\text{sph}}, r_{\text{sph}} \sin \theta_{\text{sph}} \sin \phi_{\text{sph}}, r_{\text{sph}} \cos \theta_{\text{sph}}). \quad (3.24)$$

2. Identify the Boyer-Lindquist coordinates with flat-space oblate-spheroidal coordinates $\{r_{\text{BL}}, \theta_{\text{BL}}, \phi_{\text{BL}}\} \rightarrow \{r_{\text{ob}}, \theta_{\text{ob}}, \phi_{\text{ob}}\}$ so that the flat-space Cartesian coordinates

are

$$\mathbf{x} = \left(\sqrt{r_{\text{ob}}^2 + a^2} \sin \theta_{\text{ob}} \cos \phi_{\text{ob}}, \sqrt{r_{\text{ob}}^2 + a^2} \sin \theta_{\text{ob}} \sin \phi_{\text{ob}}, r_{\text{ob}} \cos \theta_{\text{ob}} \right). \quad (3.25)$$

These are appealing because in the limit that $G \rightarrow 0$, so that the gravitating mass goes to zero, the Kerr metric in Boyer-Lindquist coordinates reduces to the Minkowski metric in oblate-spheroidal coordinates.

In the limit of $a \rightarrow 0$, the two coincide, as they do in the limit of large r_{BL} . It must be stressed that there is no well motivated argument that either coordinate system must yield an accurate GW; their use is justified *post facto* by comparison with results obtained from more accurate, and computationally intensive, methods^[70, 78]. The ambiguity in assigning flat-space coordinates reflects the inconsistency of the semi-relativistic approximation: the geodesic trajectory was calculated for the Kerr geometry; by moving to flat spacetime we lose the reason for its existence. However, this inconsistency should not be regarded as a major problem; it is just an artifact of the basic assumption that the shape of the trajectory is important for determining the character of the radiation, but the curvature of the spacetime in the vicinity of the source is not. By binding the particle to the exact geodesic, we ensure that the kludge waveform has spectral components at the correct frequencies, but by assuming flat spacetime for generation of GWs they will not have the correct amplitudes.

3.3.2 Quadrupole-Octopole Formula

Now we have a flat-space particle trajectory $x_p^\mu(\tau)$, we may apply a flat-space wave generation formula. We shall use the quadrupole-octopole formula to calculate the gravitational strain^[81, 82]

$$h^{jk}(t, \mathbf{x}) = -\frac{2G}{c^6 r} \left[\ddot{I}^{jk} - 2n_i \ddot{S}^{ijk} + n_i \ddot{M}^{ijk} \right]_{t'=t-r/c} \quad (3.26)$$

where an over-dot represents differentiation with respect to time t (and not τ), t' is the retarded time, $r = |\mathbf{x} - \mathbf{x}_p|$ is the radial distance, \mathbf{n} is the radial unit vector, and the mass quadrupole I^{jk} , current quadrupole S^{ijk} and mass octopole M^{ijk} are defined by

$$I^{jk}(t') = \int x'^j x'^k T^{00}(t', \mathbf{x}') d^3 x'; \quad (3.27)$$

$$S^{ijk}(t') = \int x'^j x'^k T^{0i}(t', \mathbf{x}') d^3 x'; \quad (3.28)$$

$$M^{ijk}(t') = \frac{1}{c} \int x'^i x'^j x'^k T^{00}(t', \mathbf{x}') d^3 x'. \quad (3.29)$$

This is correct for a slow moving source. It is the familiar quadrupole formula^[1, 32], derived from linearized theory plus the next order terms. For a point mass the energy-momentum tensor $T^{\mu\nu}$ contains a δ -function which allows easy evaluation of the integrals

of the various moments to give

$$I^{jk} = c^2 \mu x_p^j x_p^k, \quad (3.30)$$

$$S^{ijk} = c \mu v_p^i x_p^j x_p^k, \quad (3.31)$$

$$M^{ijk} = c \mu x_p^i x_p^j x_p^k. \quad (3.32)$$

Since we are only interested in GWs, we shall use the transverse-traceless (TT) gauge. The waveform is given in the TT gauge by^[1]

$$h_{jk}^{\text{TT}} = P_j^l h_{lm} P_k^m - \frac{1}{2} P_{jk} P^{lm} h_{lm}, \quad (3.33)$$

where the (spatial) projection operator P_{ij} is

$$P_{ij} = \delta_{ij} - n_i n_j. \quad (3.34)$$

3.4 Detection With LISA

The LISA detector is a three arm, space-borne laser interferometer^[7,8]. The three arms form an equilateral triangle that rotates as the system's centre of mass follows a circular, heliocentric orbit, trailing 20° behind the Earth. To describe the detector configuration, and to transform from the MBH coordinate system to those of the detector, we will find it useful to define three coordinate systems: those of the BH at the GC x_\bullet^i ; ecliptic coordinates centred at the solar system (SS) barycentre x_\odot^i , and coordinates that co-rotate with the detector x_d^i . The MBH's coordinate system and the SS coordinate system are depicted in figure 3.2. The currently envisioned LISA mission geometry is

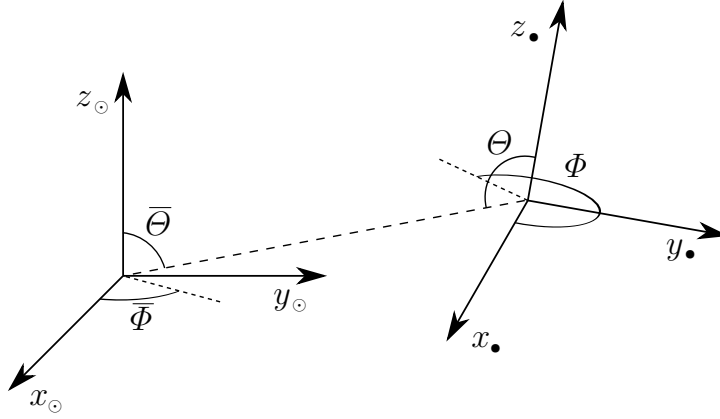


Figure 3.2: The relationship between the MBH's coordinate system x_\bullet^i and the SS coordinate system x_\odot^i . The MBH's spin axis is aligned with the z_\bullet -axis.

shown in figure 3.3. We define the detector coordinates such that the detector-arms lie in the x_d - y_d plane as shown in figure 3.4. The coordinate systems are related by a series of angles: Θ and Φ give the orientation of the SS in the MBH's coordinates. These

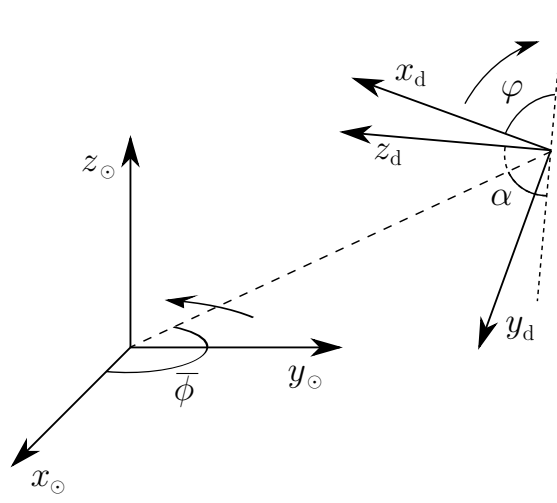


Figure 3.3: The relationship between the detector coordinates x_d^i and the ecliptic coordinates of the SS x_\odot^i [7].

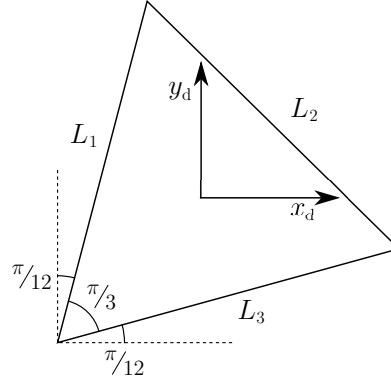


Figure 3.4: The alignment of the three detector arms, with lengths L_1 , L_2 and L_3 , within the x_d - y_d plane^[83]. The origin of the detector coordinates coincides with the centre of mass of the constellation of satellites.

define the orientation of the MBH's spin axis z_\bullet . $\bar{\Theta}$ and $\bar{\Phi}$ give the position of the GC in ecliptic coordinates.³ $\bar{\phi}$ gives LISA's orbital phase and φ gives the rotational phase of the detector arms. Both of these vary linearly with time

$$\bar{\phi}(t) = \omega_\oplus t + \bar{\phi}_0; \quad \varphi(t) = -\omega_\oplus t + \varphi_0; \quad (3.35)$$

where ω_\oplus corresponds to one rotation per year. Finally, $\alpha = 60^\circ$ is the inclination of the detector plane. We have computed the waveforms in the MBH's coordinates,

³Note added in proof: There needs to be an additional angle Ψ to specify the orientation of the axes in the plane of the sky. This will be included in future work.

however it is simplest to describe the measured signal using the detector's coordinates. To transform between coordinates we will use the matrix A_{ij} :

$$x_{\text{d}}^i = A_j^i x_{\bullet}^j; \quad h_{\text{d}}^{ij} = A_k^i A_l^j h_{\bullet}^{kl}. \quad (3.36)$$

To define this, it is convenient to introduce angles

$$\Sigma = \bar{\Theta} + \Theta; \quad \delta = \bar{\phi} - \bar{\Phi}. \quad (3.37)$$

The transformation matrix from the BH coordinates to the detector coordinates is

$$\left[A_j^i \right] = \begin{bmatrix} a_{11} & a_{12} & a_{13} \\ a_{21} & a_{22} & a_{23} \\ a_{31} & a_{32} & a_{33} \end{bmatrix}; \quad (3.38)$$

with elements

$$a_{11} = s_{\varphi} (c_{\delta} s_{\Phi} - s_{\delta} c_{\Phi} c_{\Sigma}) - c_{\varphi} [s_{\alpha} c_{\Phi} s_{\Sigma} - c_{\alpha} (c_{\delta} c_{\Phi} c_{\Sigma} + s_{\delta} s_{\Sigma})]; \quad (3.39)$$

$$a_{12} = -s_{\varphi} (c_{\delta} c_{\Phi} - s_{\delta} s_{\Phi} c_{\Sigma}) - c_{\varphi} [s_{\alpha} s_{\Phi} s_{\Sigma} - c_{\alpha} (c_{\delta} s_{\Phi} c_{\Sigma} + s_{\delta} s_{\Sigma})]; \quad (3.40)$$

$$a_{13} = s_{\varphi} s_{\delta} s_{\Sigma} - c_{\varphi} (s_{\alpha} c_{\Sigma} + c_{\alpha} c_{\delta} s_{\Sigma}); \quad (3.41)$$

$$a_{21} = s_{\varphi} [s_{\alpha} c_{\Phi} s_{\Sigma} - c_{\alpha} (c_{\delta} c_{\Phi} c_{\Sigma} + s_{\delta} s_{\Sigma})] - c_{\varphi} (c_{\delta} s_{\Phi} - s_{\delta} c_{\Phi} s_{\Sigma}); \quad (3.42)$$

$$a_{22} = s_{\varphi} [s_{\alpha} s_{\Phi} s_{\Sigma} - c_{\alpha} (c_{\delta} s_{\Phi} c_{\Sigma} + s_{\delta} s_{\Sigma})] - c_{\varphi} (c_{\delta} c_{\Phi} - s_{\delta} s_{\Phi} s_{\Sigma}); \quad (3.43)$$

$$a_{23} = s_{\varphi} (s_{\alpha} c_{\Sigma} + c_{\alpha} c_{\delta} s_{\Sigma}) - c_{\varphi} s_{\delta} s_{\Sigma}; \quad (3.44)$$

$$a_{31} = -s_{\alpha} (c_{\delta} c_{\Phi} c_{\Sigma} + s_{\delta} s_{\Phi}) - c_{\alpha} c_{\Phi} s_{\Sigma}; \quad (3.45)$$

$$a_{32} = s_{\alpha} (s_{\delta} c_{\Phi} - c_{\delta} s_{\Phi} c_{\Sigma}) - c_{\alpha} s_{\Phi} s_{\Sigma}; \quad (3.46)$$

$$a_{33} = s_{\alpha} c_{\delta} s_{\Sigma} - c_{\alpha} c_{\Sigma}; \quad (3.47)$$

where we define $s_{\vartheta} \equiv \sin \vartheta$ and $c_{\vartheta} \equiv \cos \vartheta$.

The strains measured in the three arms can be combined such that LISA behaves as a pair of 90° interferometers at 45° to each other (with signals scaled by $\sqrt{3}/2$)^[83]. We will denote the two detectors as I and II. If we label the change in the three arms' lengths caused by GWs δL_1 , δL_2 and δL_3 , and use L for the unperturbed length, then detector I measures strain

$$h_{\text{I}}(t) = \frac{\delta L_1 - \delta L_2}{L} \quad (3.48)$$

$$= \frac{\sqrt{3}}{2} \left(\frac{1}{2} h_{\text{d}}^{xx} - \frac{1}{2} h_{\text{d}}^{yy} \right), \quad (3.49)$$

and detector II measures

$$h_{\text{II}}(t) = \frac{\delta L_1 + \delta L_2 - 2\delta L_3}{\sqrt{3}L} \quad (3.50)$$

$$= \frac{\sqrt{3}}{2} \left(\frac{1}{2} h_{\text{d}}^{xy} + \frac{1}{2} h_{\text{d}}^{yx} \right). \quad (3.51)$$

We will use vector notation $\mathbf{h}(t) = (h_{\text{I}}(t), h_{\text{II}}(t)) = \{h_A(t)\}$ to represent signals from both detectors.

The final consideration for calculating the signal measured by LISA is the time of arrival of the signal: LISA's orbital position changes with time. Fortunately over the timescales of interest for parabolic encounters, these changes are small. We will assume that the position of the SS barycentre relative to the GC is constant, at least over these short timescales: it is defined by the distance R_0 and the angles $\bar{\Theta}$ and $\bar{\Phi}$. The time of arrival at the SS barycentre t_\odot is then the appropriate retarded time. The time of detection t_d to lowest order is then

$$t_d \simeq t_\odot - t_{\text{AU}} \cos \left[\bar{\phi}(t_\odot) - \bar{\Phi} \right] \sin \bar{\Theta}, \quad (3.52)$$

where t_{AU} is the light travel-time for LISA's orbital radius. The time t_d must be used for $\phi(t)$ and $\varphi(t)$.

3.5 Signal Analysis

3.5.1 Frequency Domain Formalism

At this stage we now know the GW $\mathbf{h}(t)$ that will be incident upon the LISA detector. We must now discuss how to analyse the waveform to extract the information it contains. We begin with a brief overview of the basic components of signal analysis used for GWs, with application to LISA in particular. This fixes notation. A more complete discussion of the material can be found in the work of Finn^[84], and Cutler and Flanagan^[85].

The actual measured strain $\mathbf{s}(t)$ will be the combination of the signal and the detector noise

$$\mathbf{s}(t) = \mathbf{h}(t) + \mathbf{n}(t); \quad (3.53)$$

we will assume that the noise $n_A(t)$ is stationary and Gaussian. When analysing signals, it is most convenient to work with the Fourier transform

$$\tilde{g}(f) = \int_{-\infty}^{\infty} g(t) e^{2\pi i f t} dt. \quad (3.54)$$

Since we have assumed Gaussianity for the noise signal $n_A(t)$, each Fourier component $\tilde{n}_A(f)$ also has a Gaussian probability distribution; the assumption of stationarity means that different Fourier components are uncorrelated, thus^[85]

$$\langle \tilde{n}_A(f) \tilde{n}_B^*(f') \rangle_n = \frac{1}{2} \delta(f - f') S_{AB}(f), \quad (3.55)$$

where $\langle \dots \rangle_n$ denotes the expectation value over the noise distribution, and $S_{AB}(f)$ is the (single-sided) noise spectral density. For simplicity, we may assume that the noise in the two detectors is uncorrelated, but share the same characterization so that^[83]

$$S_{AB}(f) = S_n(f) \delta_{AB}. \quad (3.56)$$

The functional form of the noise spectral density $S_n(f)$ for LISA is discussed in section 3.5.2.

The properties of the noise allow us to define a natural inner product and associated distance on the space of signals^[85]

$$(\mathbf{g}|\mathbf{k}) = 2 \int_0^\infty \frac{\tilde{g}_A^*(f)\tilde{k}_A(f) + \tilde{g}_A(f)\tilde{k}_A^*(f)}{S_n(f)} df. \quad (3.57)$$

Using this definition, the signal-to-noise ratio (SNR) is approximately

$$\rho[\mathbf{h}] = (\mathbf{h}|\mathbf{h})^{1/2}. \quad (3.58)$$

The probability of a particular realization of noise $\mathbf{n}(t) = \mathbf{n}_0(t)$ is

$$p(\mathbf{n}(t) = \mathbf{n}_0(t)) \propto \exp \left[-\frac{1}{2} (\mathbf{n}_0|\mathbf{n}_0) \right]. \quad (3.59)$$

If the incident waveform is given as $\mathbf{h}(t)$, the probability of measuring signal $\mathbf{s}(t)$ is

$$p(\mathbf{s}(t)|\mathbf{h}(t)) \propto \exp \left[-\frac{1}{2} (\mathbf{s} - \mathbf{h}|\mathbf{s} - \mathbf{h}) \right]. \quad (3.60)$$

3.5.2 LISA Noise Curve

LISA's noise has two sources: instrumental noise and confusion noise, primarily from white dwarf binaries. The latter may be divided into contributions from galactic and extragalactic binaries. In this work we use the noise model of Barack and Cutler^[86]. The shape of the noise curve can be seen in figure 3.5. The instrumental noise dominates at both high and low frequencies. The confusion noise is important at intermediate frequencies, and is responsible for the cusp around $f = 1 \times 10^{-3}$ Hz.

3.5.3 Window Functions

There is one remaining complication: since we are Fourier transforming a finite signal we encounter spectral leakage; a contribution from large amplitude spectral components leaks into other components (sidelobes), obscuring and distorting the spectrum at these frequencies^[87,88]. This is an inherent problem with finite signals; it will be as much of a problem when analysing signals from LISA as it is computing waveforms here. However, it is possible to reduce the amount of spectral leakage using apodization: to improve the frequency response of a finite time series one can use a number of weighting window functions $w(t)$ which modify the impulse response in a prescribed way. There is a wide range of window functions described in the literature^[88-90]. Figure 3.6 shows the computed Fourier transforms for an example parabolic encounter using no window (alternatively a rectangular or Dirichlet window), and the Nuttall 4-term window with continuous first derivative^[90].⁴ The waveforms have two distinct regions: a low-frequency curve, and a high-frequency tail. The low-frequency signal is the spectrum we are interested in; the high-frequency components are the result of spectral leakage. Using the

⁴The Blackman-Harris minimum 4-term window^[88,90], and the Kaiser-Bessel window^[88,89] give almost identical results.

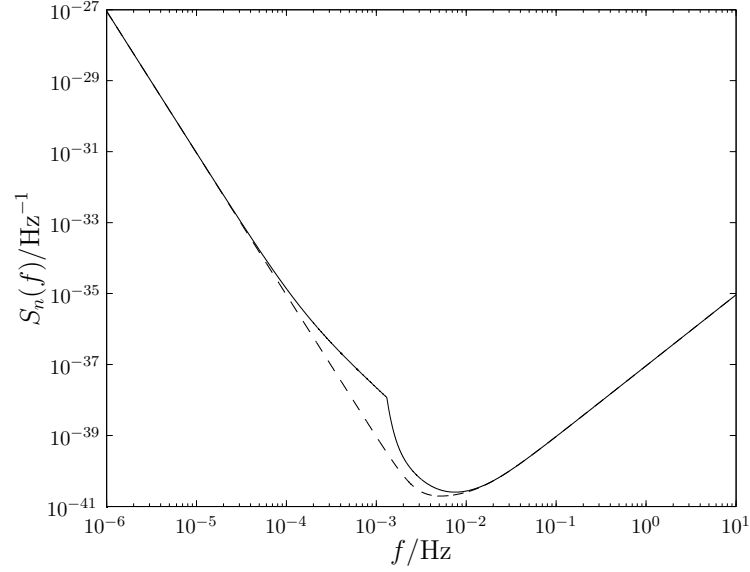


Figure 3.5: Approximate noise curve for LISA^[86]. The solid line includes both instrumental and confusion noise, the dashed line shows only instrumental.

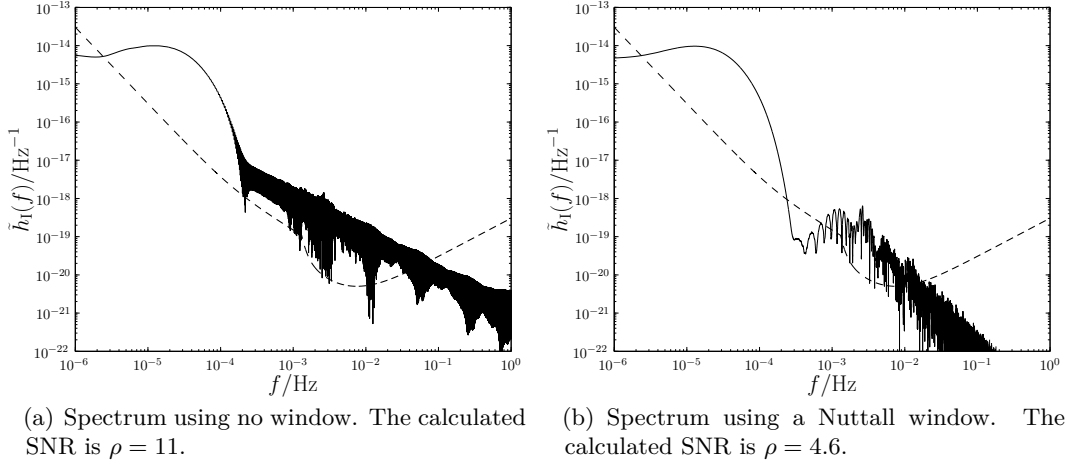


Figure 3.6: Example spectra calculated using (a) a rectangular window and (b) Nuttall's 4-term window with continuous first derivative^[90]. The input parameters are: $M_{\bullet} = 4.3 \times 10^6 M_{\odot}$, $a = 0.5 M_{\bullet}$, $\Theta = \pi/3$, $\Phi = 0$, $R_0 = 8.33$ kpc, $\bar{\Theta} = 95.607669^\circ$, $\bar{\Phi} = 266.851760^\circ$, $\bar{\phi}_0 = 0$, $\varphi_0 = 0$, $L_z = 10.44 M_{\bullet}$, $Q = 0.055 M_{\bullet}^2$, $\mu = 5 M_{\odot}$, $x_0 = 3.5 \times 10^{12}$ m, $y_0 = 3.0 \times 10^{12}$ m, $z_0 = 1.0 \times 10^{11}$ m; see section 3.6.1 for a discussion of these parameters. The periape distance is $r_p = 52.7 M_{\bullet}$. The high-frequency tail is the result of spectral leakage. The level of the LISA noise curve is indicated by the dashed line. The spectra are from detector I, detector II has similar spectra.

Nuttall window, the spectral leakage is greatly reduced; the peak sidelobe is lower, and the tail decays away as $1/f^3$ instead of $1/f$. This window is used for all future waveforms.

We must use a windowing function as despite being many orders of magnitude below the peak level, the high-frequency tail is still well above the noise curve for a wide range of frequencies. It will therefore contribute to the evaluation of any inner products, and may mask interesting features at these frequencies.

3.6 Parameter Estimation & Waveforms

3.6.1 Model Parameters

The shape of the waveform depends on a number of parameters: those defining the MBH; those defining the companion object on its orbit, and those defining the LISA detector. Let us define $\lambda = \{\lambda^1, \lambda^2, \dots, \lambda^N\}$ as the set of N parameters which specify the GW. For our model the input parameters are:

1. The MBH's mass M_\bullet . This is currently well constrained by the observation of stellar orbits about Sgr A*^[58, 91], with the best estimate being $M_\bullet = (4.31 \pm 0.36) \times 10^6 M_\odot$. However this depends upon the galactic centre distance R_0 being accurately known. If the uncertainty in this is included $M_\bullet = (3.95 \pm 0.06)_{\text{stat}} \pm 0.18|_{R_0, \text{stat}} \pm 0.31|_{R_0, \text{sys}} \times 10^6 M_\odot (R_0/8 \text{ kpc})^{2.19}$, where the errors are statistical, independent of R_0 ; statistical from the determination of R_0 , and systematic from R_0 .
2. The spin parameter a . Naively this could be anywhere in the range $|a| < M_\bullet$, however it may be limited by the accretion history. Considering the torque from radiation emitted by an accretion disc and swallowed by the BH it may be argued that $|a| \lesssim 0.998 M_\bullet$ ^[92]. If the MBH grew via a series of randomly orientated accretion events, then the spin parameter can be low, and we expect an average value $|a| \sim 0.1\text{--}0.3 M_\bullet$ ^[93, 94].
3. The polar angle Θ defining the propagation direction.
4. The SS-GC distance R_0 . As for M_\bullet , this is constrained by stellar orbits, the best estimate being^[58] $R_0 = (8.33 \pm 0.35) \text{ kpc}$.
- 5, 6. The coordinates of the MBH from the SS barycentre $\bar{\Theta}$ and $\bar{\Phi}$. These may be taken as the coordinates of Sgr A*, as the radio source is expected to be within ten Schwarzschild radii of the MBH^[95, 96]. At the epoch J2000.0^[97] $\bar{\Theta} = 95.607669^\circ$, $\bar{\Phi} = 266.851760^\circ$. This will change with time due to the rotation of the SS about the GC, the proper motion is about 6 mas yr^{-1} , mostly in the plane of the galaxy^[95, 97, 98].
7. The angular momentum of the orbit about the MBH's spin axis L_z .
8. The Carter constant for the orbit Q .

9. The mass of the orbiting particle μ . This will depend upon the type of object: whether it is a MS star, WD, NS or BH.
- 10–12. The initial position of the particle (x_0, y_0, z_0) . For specific values of Q and L_z there is a definite upper limit on $|z_0|/\sqrt{x_0^2 + y_0^2}$ given by the size of θ_0 from equation (3.20).
- 13, 14. The orbital position of the LISA satellites given by $\bar{\phi}$ and φ .

The azimuthal angle Φ is omitted, since it arbitrarily defines the orientation of the MBH's x - and y -axes. We shall define it to be zero without loss of generality. We thus have a 14-dimensional parameter space. However, for a given signal arrival time the orbital parameters of LISA will be known; we will not try to infer these. In lieu of anything better, we will assume fiducial initial values of $\bar{\phi}_0 = 0$, $\varphi_0 = 0$.⁵ This leaves us with a 12-dimensional parameter space to explore.

3.6.2 Waveforms

Figures 3.7–3.11 show example waveforms to demonstrate some of the possible variations in the signal. All these assume $M_\bullet = 8.6 \times 10^{31} \text{ kg} \simeq 4.3 \times 10^6 M_\odot$, $R_0 = 8.33 \text{ kpc}$, $\bar{\Theta} = 95.607669^\circ$, $\bar{\Phi} = 266.851760^\circ$ and $\mu = 1 \times 10^{31} \text{ kg} \simeq 5M_\odot$; other parameters are specified in the captions. The orbits specified in figures 3.7, 3.8 and 3.10 all loop once

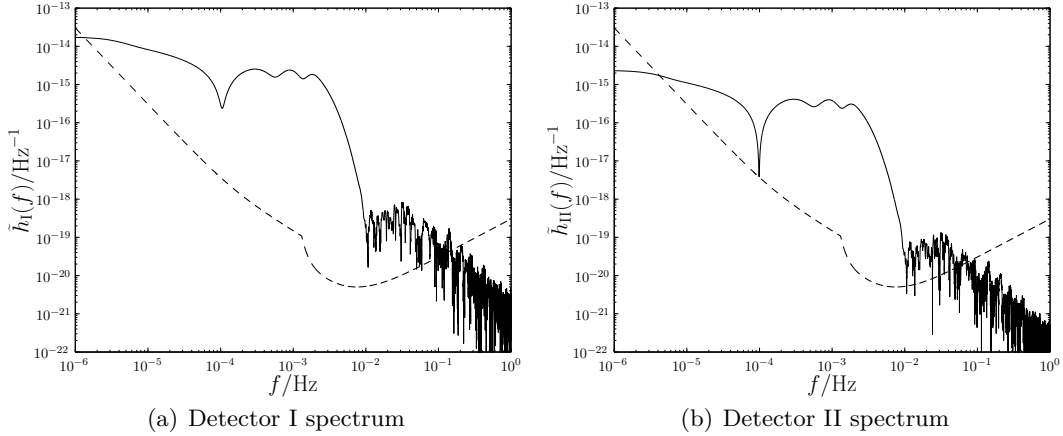


Figure 3.7: Waveform for model parameters: $a = 0.5M_\bullet$, $\Theta = \pi/3$, $L_z = 3.67M_\bullet$, $Q = 0.409M_\bullet^2$, $x_0 = 3.0 \times 10^{12} \text{ m}$, $y_0 = 4.0 \times 10^{12} \text{ m}$, $z_0 = 2.0 \times 10^{11} \text{ m}$. The periaapse distance is $r_p = 4.67M_\bullet$, the SNR is $\rho = 8800$.

⁵The values of $\bar{\phi}_0$ and φ_0 do change the observed waveforms, altering the strain measured in the two arms. We do not investigate the full implications of this since we already have a large number of variables to consider, and because we will not know how $\bar{\phi}$ and φ will be related until the mission geometry is finalised.

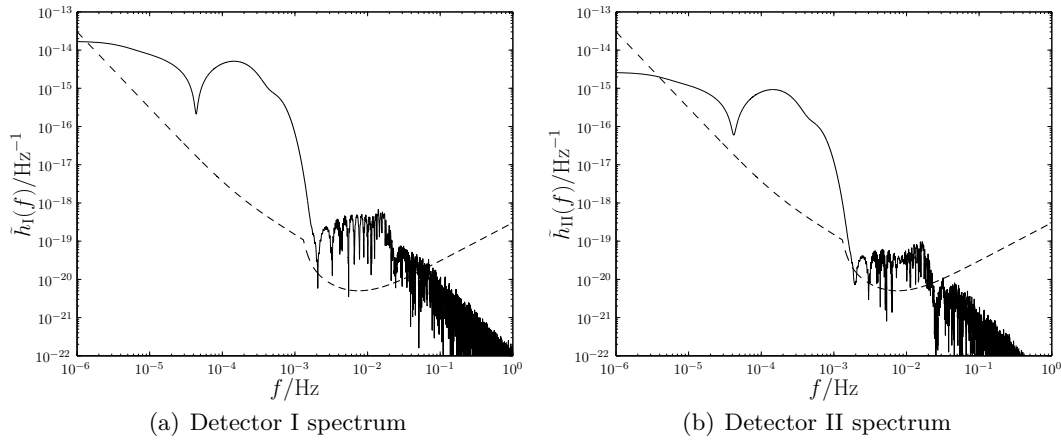


Figure 3.8: Waveform for model parameters: $a = 0.5M_\bullet$, $\Theta = \pi/3$, $L_z = 5.22M_\bullet$, $Q = 0.055M_\bullet^2$, $x_0 = 3.5 \times 10^{12}$ m, $y_0 = 3.5 \times 10^{12}$ m, $z_0 = 1.0 \times 10^{11}$ m. The periaapse distance is $r_p = 11.77M_\bullet$, the SNR is $\rho = 140$.

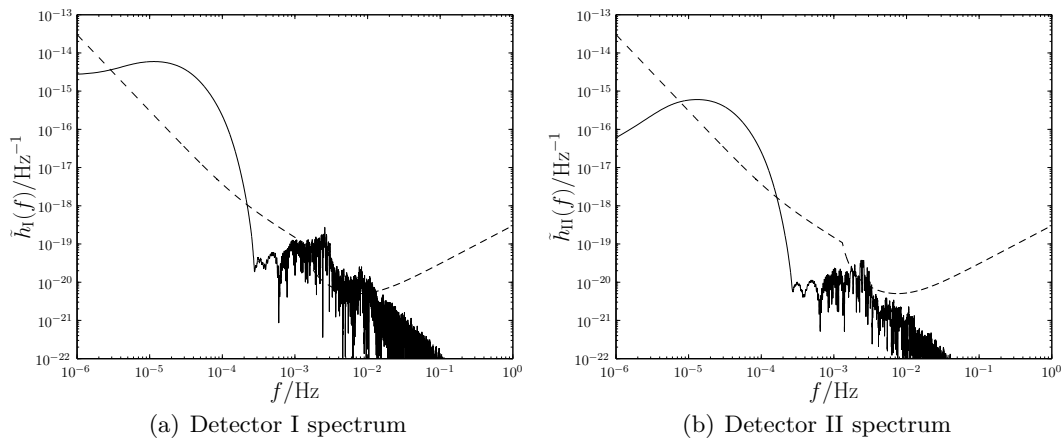


Figure 3.9: Waveform for model parameters: $a = 0.2M_\bullet$, $\Theta = \pi/2$, $L_z = 10.45M_\bullet$, $Q = 2.18M_\bullet^2$, $x_0 = 3.5 \times 10^{12}$ m, $y_0 = 3.5 \times 10^{12}$ m, $z_0 = 5.0 \times 10^{11}$ m. The periaapse distance is $r_p = 53.7M_\bullet$, the SNR is $\rho = 2.2$.

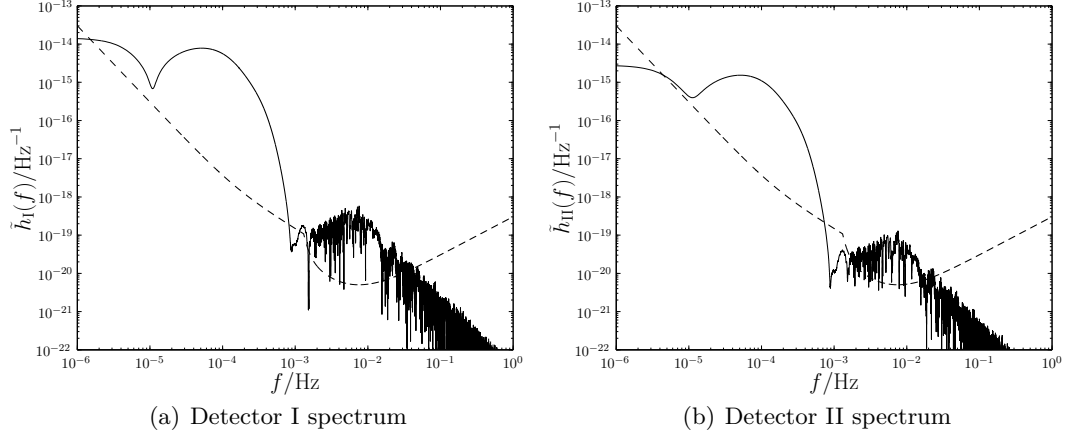


Figure 3.10: Waveform for model parameters: $a = 0.7M_\bullet$, $\Theta = \pi/2$, $L_z = 5.22M_\bullet$, $Q = 21.8M_\bullet^2$, $x_0 = 2.8 \times 10^{12} \text{ m}$, $y_0 = 2.8 \times 10^{12} \text{ m}$, $z_0 = 3.0 \times 10^{12} \text{ m}$. The periaapse distance is $r_p = 22.7M_\bullet$, the SNR is $\rho = 44$.

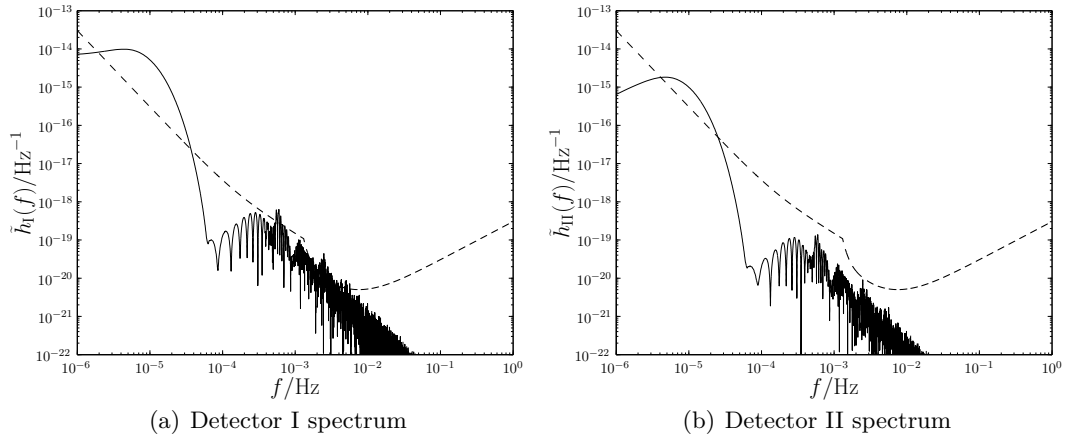


Figure 3.11: Waveform for model parameters: $a = 0.7M_\bullet$, $\Theta = \pi/2$, $L_z = 15.7M_\bullet$, $Q = 84.6M_\bullet^2$, $x_0 = 1.0 \times 10^{12} \text{ m}$, $y_0 = 4.2 \times 10^{12} \text{ m}$, $z_0 = 1.0 \times 10^{12} \text{ m}$. The periaapse distance is $r_p = 148M_\bullet$, the SNR is $\rho = 0.18$.

about the MBH — they are the simplest zoom-whirl orbits. The others, including the orbit of figure 3.6, are simpler trajectories that are recognisable as parabolic in shape. There is a clear distinction between the two types of orbit, as the loops introduce higher frequency harmonics.

The plotted waveforms use the oblate-spheroidal coordinate system for the NK. Using spherical polars makes negligible difference: on the scale shown here the only discernible difference would be in the spikes of the high-frequency tail of the orbits with smaller periapses, and even that is minor. We conclude that the choice of coordinates for the kludge approximation is unimportant, and shall continue using oblate-spheroidal coordinates for the rest of this work.

3.6.3 Inference & Fisher Matrices

Having detected a GW signal $\mathbf{s}(t)$ we are interested in what we can learn about the source. We have an inference problem that can be solved by appropriate application of Bayes' Theorem^[99]: the probability distribution for our parameters given that we have detected the signal $\mathbf{s}(t)$ is given by the posterior

$$p(\boldsymbol{\lambda}|\mathbf{s}(t)) = \frac{p(\mathbf{s}(t)|\boldsymbol{\lambda})p(\boldsymbol{\lambda})}{p(\mathbf{s}(t))}. \quad (3.61)$$

Here $p(\mathbf{s}(t)|\boldsymbol{\lambda})$ is the likelihood of the parameters, $p(\boldsymbol{\lambda})$ is the prior probability distribution for the parameters, and $p(\mathbf{s}(t)) = \int p(\mathbf{s}(t)|\boldsymbol{\lambda}) d^N \lambda$ is, for our purposes, a normalising constant and may be ignored. The likelihood function depends upon the realization of noise. A particular set of parameters $\boldsymbol{\lambda}_0$ defines a waveform $\mathbf{h}_0(t) = \mathbf{h}(t; \boldsymbol{\lambda}_0)$, the probability that we observe signal $\mathbf{s}(t)$ for this GW is given by equation (3.60), so the likelihood is

$$p(\mathbf{s}(t)|\boldsymbol{\lambda}_0) \propto \exp \left[-\frac{1}{2} (\mathbf{s} - \mathbf{h}_0 | \mathbf{s} - \mathbf{h}_0) \right]. \quad (3.62)$$

If we were to define this as a probability distribution for the parameters $\boldsymbol{\lambda}$, then the modal values would be the maximum-likelihood parameters $\boldsymbol{\lambda}_{\text{ML}}$. The waveform $\mathbf{h}(t; \boldsymbol{\lambda}_{\text{ML}})$ would be the signal closest to $\mathbf{s}(t)$ in the space of all signals, where distance is defined using the inner product equation (3.57)^[85].

In the limit of a high SNR, we may approximate this as^[100]

$$p(\mathbf{s}(t)|\boldsymbol{\lambda}_0) \propto \exp \left[-\frac{1}{2} (\partial_a \mathbf{h} | \partial_b \mathbf{h}) (\lambda^a - \langle \lambda^a \rangle_\ell) (\lambda^b - \langle \lambda^b \rangle_\ell) \right], \quad (3.63)$$

where the mean is defined as

$$\langle \lambda^a \rangle_\ell = \frac{\int \lambda^a p(\mathbf{s}(t)|\boldsymbol{\lambda}) d^N \lambda}{\int p(\mathbf{s}(t)|\boldsymbol{\lambda}) d^N \lambda}. \quad (3.64)$$

Using the high SNR limit, this is the maximum-likelihood value $\langle \lambda^a \rangle_\ell = \lambda_{\text{ML}}^a$. The quantity

$$\Gamma_{ab} = (\partial_a \mathbf{h} | \partial_b \mathbf{h}) \quad (3.65)$$

is the Fisher information matrix. It controls the variance of the likelihood distribution.

The form of the posterior distribution will depend upon the nature of the prior information. If we have an uninformative prior, such that $p(\boldsymbol{\lambda})$ is a constant, then the posterior distribution would be determined by the likelihood. In the high SNR limit, we would obtain a Gaussian with variance-covariance matrix

$$\boldsymbol{\Sigma} = \boldsymbol{\Gamma}^{-1}. \quad (3.66)$$

The Fisher information matrix gives the uncertainty associated with the estimated parameter values, in this case the maximum-likelihood values.

If the prior were to restrict the allowed range for a parameter, for example, as is the case for the spin a , then the posterior would be a truncated Gaussian, and $\boldsymbol{\Gamma}^{-1}$ would no longer represent the variance-covariance.

If the prior were approximately Gaussian with variance-covariance matrix $\boldsymbol{\Sigma}_0$, then the posterior would also be Gaussian.⁶ The posterior variance-covariance would be^[85, 100]

$$\boldsymbol{\Sigma} = \left(\boldsymbol{\Gamma} + \boldsymbol{\Sigma}_0^{-1} \right)^{-1}. \quad (3.67)$$

From this the inverse Fisher matrix $\boldsymbol{\Gamma}^{-1}$ is an upper bound on the size of the posterior covariance matrix.⁷

As a first estimate of what we may learn from parabolic encounters we have only looked at the inverse Fisher matrix elements. If these are small then we expect we would be able to precisely determine a parameter, whereas if they are large we would not be able to learn much more than we already know from our prior.

3.6.4 Inverse Fisher Matrices

Calculating the inverse Fisher matrix for example orbits, we find that there is a large degeneracy between the mass μ and the distance R_0 . This is not surprising since the primary role of both is determining the amplitude of the waveform in equation (3.26). This is the only place that μ appears. We cannot determine both from an extreme mass-ratio burst, unless we can determine the mass of the object by other means, which seems unlikely. It appears that we must give up on determining R_0 . Instead we should accept our prior value and remove R_0 from the parameter set.

The inverse Fisher matrix's elements for some example orbits are tabulated in the appendix. For the values presented here the parameters are normalised with respect to their maximum likelihood values $\hat{\lambda}^a = \lambda^a / \lambda_{\text{ML}}^a$; the Fisher matrices are calculated by differentiating with respect to these parameters so that $\boldsymbol{\Gamma}^{-1}$ gives the relative variance-covariance.

There are a few general properties. The parameters M_\bullet and Θ always have relatively small variances. These parameters are crucial for defining the BH system: M_\bullet sets the

⁶If we only know the typical value and spread of a parameter then a Gaussian is the maximum entropy prior^[99]: the prior that is least informative given what we do know.

⁷It may also be shown to be the Cramér-Rao bound on the error covariance of an unbiased estimator^[85, 100]. Thus it represents the frequentist error: the lower bound on the covariance for an unbiased parameter estimator $\boldsymbol{\lambda}_{\text{est}}$ calculated from an infinite set of experiments with the same signal $\mathbf{h}(t)$ but different realizations of the noise $\mathbf{n}(t)$.

scale for the system and Θ the orientation. If a were small, the spacetime would be almost spherically symmetric and we would expect a large variance for Θ . The angular momentum L_z also has a small variance, it is important for specifying the orbit; its partner Q , however, does not always have a small variance, in fact in some cases it has one of the largest. This appears to correlate with the sizes of the covariances of Q : the orbits with the smallest periapses have relatively large covariances for the set of parameters $\{a, Q, z_0\}$, indicating that there is some degeneracy between these. In these cases Q has a much larger variance, as does z_0 . The initial coordinates x_0 , y_0 and z_0 typically have small variances, the exception being the aforementioned case for z_0 .

The parameters with the largest variances are $\bar{\Theta}$ and μ . The large variance of $\bar{\Theta}$ reflects the poor angular resolution of gravitational wave detectors; $\bar{\Phi}$ has a smaller variance as a change in azimuthal position changes the waveform observed in the two detector arms. The particle mass μ has a large variance since it only alters the amplitude of the spectrum and not its shape.

The variances are smaller for larger values of the SNR as is expected. We are able to get such good values from the orbits with small periapses since they have both a high SNR and the distinctive structure of a zoom-whirl orbit.

From this preliminary look at a few example orbits, it appears that we should be able to infer the mass of the Kerr BH at the GC from an EMRB. We can gain information regarding the spin of the MBH if the orbit's periapsis is sufficiently small — we could learn nothing from the orbit of table A.6. The Fisher matrix analysis suggests that we should be able to accurately infer the spin orientation; however it seems likely that there could be difficulties for small spin values. This will require further investigation. It seems unlikely that we will be able to improve upon our current best estimate for the position of the MBH, but this is already well constrained.

What is particularly exciting is the amount of information we could obtain from a single encounter, which may be all that we would have the opportunity to observe with LISA. Taking the results of table A.1, which are for an orbit of periapsis $r_p = 52.7M_\bullet$, as an example, we could infer maximum-likelihood values $M_\bullet = (4.32 \pm 0.07) \times 10^6 M_\odot$, $a = (0.50 \pm 0.02)M_\bullet$, and $\Theta = (60.0 \pm 1.6)^\circ$. Here we have ignored uncertainty introduced by the error in R_0 which will increase the uncertainty; however, we have also only considered information from GWs and not considered additional information from our prior knowledge: combining these as in equation (3.67) would give a smaller posterior variance. While further work will be needed to be certain how much we could expect to learn from EMRBs, this is encouraging.

3.7 Energy Spectra

To check that the NK waveforms are sensible, we may compare the energy spectra calculated from these with those obtained from the classic treatment of Peters and Matthews^[101, 102]. This calculates GW emission for Keplerian orbits in flat spacetime, assuming only quadrupole radiation. The spectrum produced should be similar to that obtained from the NK in weak fields, that is for orbits with a large periapsis; however we do not expect an exact match because of the differing input physics and various

approximations.

We do not intend to use the kludge waveforms to calculate an accurate energy flux: this would be inconsistent as we assume that the orbits do not evolve with time. We only calculate the energy flux as a sanity check; to check that the kludge approximation is consistent with other approaches.

3.7.1 Kludge Spectrum

Our gravitational wave in the TT gauge has momentum pseudotensor^[1]

$$T_{\mu\nu} = \frac{c^4}{32\pi G} \left\langle \partial_\mu h_{ij} \partial_\nu h^{ij} \right\rangle, \quad (3.68)$$

where $\langle \dots \rangle$ indicates averaging over several wavelengths or periods. The flux of energy through a sphere of radius $r = R$ is

$$\frac{dE}{dt} = \frac{c^3}{32\pi G} R^2 \int d\Omega \left\langle \frac{dh_{ij}}{dt} \frac{dh^{ij}}{dt} \right\rangle, \quad (3.69)$$

with $\int d\Omega$ representing integration over all solid angles. From equation (3.26) we see that the waves have a $1/r$ dependence; if we define

$$h_{ij} = \frac{H_{ij}}{r}, \quad (3.70)$$

we see that the flux is independent of R , as required for energy conservation,

$$\frac{dE}{dt} = \frac{c^3}{32\pi G} \int d\Omega \left\langle \frac{dH_{ij}}{dt} \frac{dH^{ij}}{dt} \right\rangle. \quad (3.71)$$

If we now integrate to find the total energy emitted we obtain

$$E = \frac{c^3}{32\pi G} \int d\Omega \int_{-\infty}^{\infty} dt \frac{dH_{ij}}{dt} \frac{dH^{ij}}{dt}. \quad (3.72)$$

Since we are considering all time, the localization of the energy is no longer of importance and it is unnecessary to average over several periods. Switching to Fourier representation $\tilde{H}_{ij}(f) = \mathcal{F}\{H_{ij}(t)\}$,

$$\begin{aligned} E &= \frac{c^3}{32\pi G} \int d\Omega \int_{-\infty}^{\infty} dt \int_{-\infty}^{\infty} df \, 2\pi i f \tilde{H}_{ij}(f) e^{2\pi i f t} \int_{-\infty}^{\infty} df' \, 2\pi i f' \tilde{H}^{ij}(f') e^{2\pi i f' t} \\ &= \frac{\pi c^3}{8G} \int d\Omega \int_{-\infty}^{\infty} df \, f^2 \tilde{H}_{ij}(f) \tilde{H}^{ij}(-f) \\ &= \frac{\pi c^3}{4G} \int d\Omega \int_0^{\infty} df \, f^2 \tilde{H}^{ij}(f) \tilde{H}_{ij}^*(f), \end{aligned} \quad (3.73)$$

using the fact that the signal is real so $\tilde{H}_{ij}^*(f) = \tilde{H}_{ij}(-f)$. From this we identify the energy spectrum as

$$\frac{dE}{df} = \frac{\pi c^3}{4G} \int d\Omega \, f^2 \tilde{H}^{ij}(f) \tilde{H}_{ij}^*(f). \quad (3.74)$$

3.7.2 Peters & Matthews Spectrum

To calculate the Peters and Matthews energy spectrum for a parabolic orbit, we use the limiting result of Gair^[103]

$$\begin{aligned} \frac{dE}{df} = \frac{4\pi^2}{5} \frac{G^3}{c^5} \frac{M_\bullet^2 \mu^2}{r_p^2} & \left\{ \left[\frac{8f^2}{f_c^2} B\left(\frac{f}{f_c}\right) - \frac{2f}{f_c} A\left(\frac{f}{f_c}\right) \right]^2 \right. \\ & \left. + \left(\frac{128f^4}{f_c^4} + \frac{4f^2}{3f_c^2} \right) \left[A\left(\frac{f}{f_c}\right) \right]^2 \right\}, \end{aligned} \quad (3.75)$$

where f_c is the orbital frequency of a circular orbit of radius equal to r_p ,

$$f_c = \frac{1}{2\pi} \sqrt{\frac{G(M_\bullet + \mu)}{r_p^3}}, \quad (3.76)$$

and functions $A(\tilde{f})$ and $B(\tilde{f})$ are defined in terms of Bessel functions. Their precise forms are

$$A(\tilde{f}) = \frac{1}{\pi} \sqrt{\frac{2}{3}} K_{1/3} \left(\frac{2^{3/2} \tilde{f}}{3} \right); \quad (3.77)$$

$$B(\tilde{f}) = \frac{1}{\sqrt{3}\pi} \left[K_{-2/3} \left(\frac{2^{3/2} \tilde{f}}{3} \right) + K_{4/3} \left(\frac{2^{3/2} \tilde{f}}{3} \right) - \frac{1}{\sqrt{2}\tilde{f}} K_{1/3} \left(\frac{2^{3/2} \tilde{f}}{3} \right) \right], \quad (3.78)$$

where $K_\nu(z)$ is a modified Bessel function of the second kind^[104].

3.7.3 Comparison

Two energy spectra are plotted in figure 3.12 for orbits with a periapsis of $r_p = 35.0r_S$, where r_S is the MBH's Schwarzschild radius. For consistency with the approximation of Peters and Matthews the NK waveform has been calculated using only the quadrupole formula. The two spectra appear to be in good agreement, showing the same general shape. The NK spectrum is more tightly peaked, but is always within a factor of 2 (ignoring the high-frequency tail).

We may also compare the total energy flux. For the orbit shown in figure 3.12 integrating the NK spectrum gives $E_{\text{NK}} = 5.936 \times 10^{36}$ J; the Peters and Matthews total energy is $E_{\text{PM}} = 5.747 \times 10^{36}$ J. The total energy flux from the kludge waveform is larger than the Peters and Matthews result. This behaviour has been seen before for high eccentricity orbits about a non-spinning BH^[78]. From the level of agreement we may be confident that the NK waveforms are a reasonable approximation.

Introducing the octopole moments makes a small change to the energy spectrum, as seen in figure 3.13. The peak of the spectrum is shifted to a slightly higher frequency, and the total energy radiated is increased to $E_{\text{NK}} = 6.202 \times 10^{36}$ J. At such radii the higher order terms only make a correction of the order of a few percent.

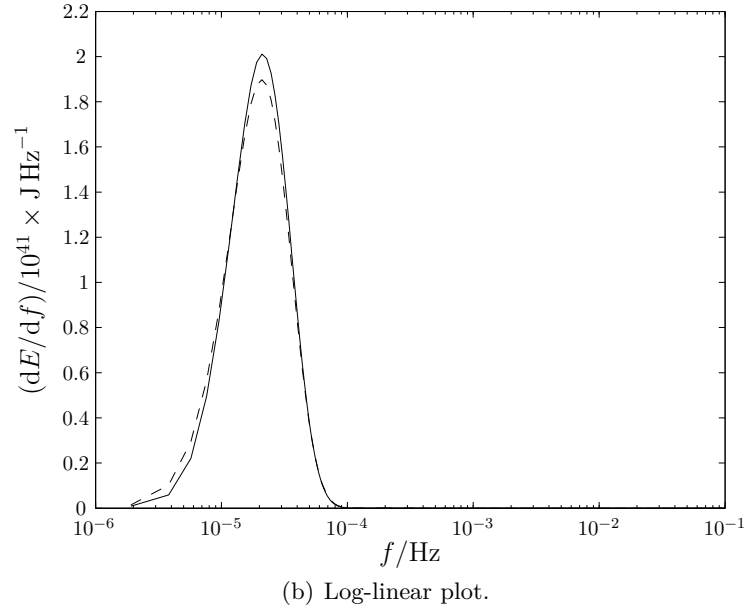
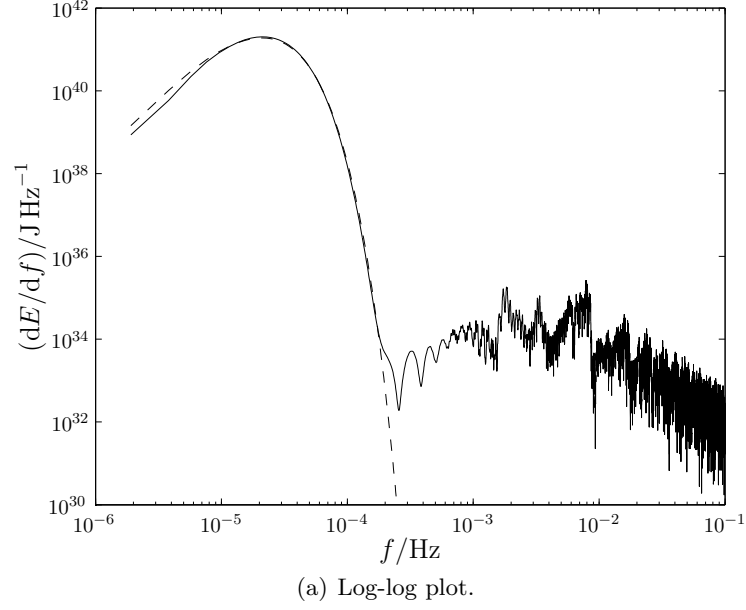
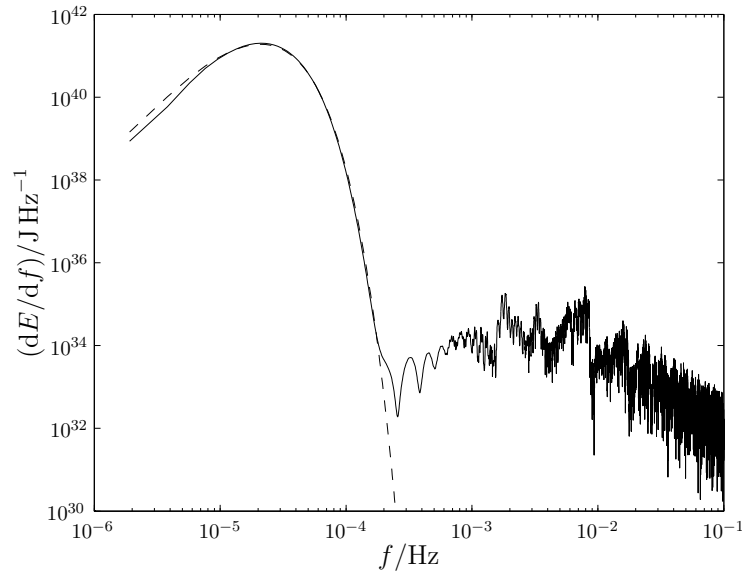
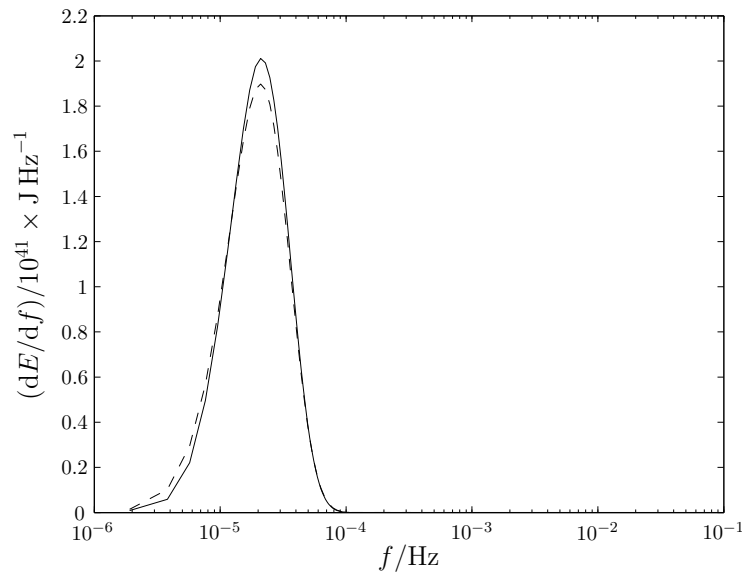


Figure 3.12: Energy spectra for a parabolic orbit of a $\mu = 1 \times 10^{31} \text{ kg} \simeq 5M_{\odot}$ object about a $M_{\bullet} = 8.6 \times 10^{36} \text{ kg} \simeq 4.3 \times 10^6 M_{\odot}$ Schwarzschild MBH with $L_z = 12M_{\bullet}$ and $Q = 0$; the periape distance is $r_p = 69.9M_{\bullet}$. The spectra calculated from a the NK waveform is shown by the solid line and the Peters and Matthews flux is indicated by the dashed line. The NK waveform only uses the quadrupole formula.



(a) Log-log plot.



(b) Log-linear plot.

Figure 3.13: Energy spectra for the same orbit as shown in figure 3.12. The spectra calculated from a the NK waveform is shown by the solid line and the Peters and Matthews flux is indicated by the dashed line. The NK waveform includes contributions from the current quadrupole and mass octopole as given by equation (3.26).

3.8 Discussion & Further Work

We have outlined an approximate method of generating gravitational waveforms for EMRBs originating at the GC. These assume that the orbit is parabolic and employs a numerical kludge approximation. The two schemes for a NK presented here yield almost indistinguishable results. The waveforms created appear to be consistent with results obtained using Peters and Matthews waveforms in the weak-field regime. The NK approach should be superior to that of Peters and Matthews in the strong-field regime as it uses exact geodesics of Kerr spacetime.

Using the NK waveforms we have conducted a trial investigation, using Fisher matrix analysis, into how accurately we could infer parameters of the galactic centre's MBH should such an EMRB be observed. Potentially, it is possible to determine very precisely the key parameters defining the MBH's mass and spin, if the orbit gets close enough to the black hole. Unfortunately it does not appear possible to infer the distance to the GC.

Before we can quote results for how accurately we can determine the various parameters, we must consider the probability of each orbit. This work would build upon the earlier results of Rubbo *et al.*^[67] and Hopman *et al.*^[68], who only considered the probability for a signal to be detectable. To calculate these probabilities it will be necessary to assume a particular dynamical model for the galactic centre so that we can define distributions for angular momenta L_z and Q , mass μ and initial position. It will also be necessary to consider on which orbits MS stars would survive without being tidally disrupted^[69]. Once the distribution of orbit parameters is known, it will be possible to assign probabilities to being able to infer parameters to a level of accuracy, for example there may be a probability $p = 0.05$ of constraining M_\bullet to within 0.01 % and a probability $p = 0.25$ of constraining M_\bullet to within 1 %. This could be done using a Monte Carlo method to sample the distribution of orbits, and calculating the variance-covariance matrix for the inferred parameters for each sample orbit. We could extend the simple Fisher matrix analysis performed here to a full Bayesian analysis with the distributions for L_z , Q , μ , x_0 , y_0 and z_0 serving as priors. However this may be too computationally expensive to justify implementing. From our preliminary investigation, which uses an extremely restricted sample of parameter space, it appears that we can achieve good results from a single EMRB with periapsis of $r_p = 50M_\bullet$. This translates to a distance of 10^{11} m or 10^{-5} pc, and therefore may be unlikely to occur within the lifetime of LISA.

Some consideration should also be given to methods of fitting a waveform to an observed signal. Given an input signal, what is the best algorithm for finding the optimal set of parameters to characterize the observed waveform? It is necessary to consider this to check if there are degenerate combinations of parameters that produce similar waveforms; if these are sufficiently distinct in parameter space we would not be aware of them by only considering the region immediately about the ML point. We do not intend to use NK waveforms to actually identify real GWs: more accurate methods should be employed for that; the point of this study would be to identify potential pitfalls that could be encountered when using accurate waveforms.

A natural continuation of this work would be to consider EMRBs from other MBHs.

LISA should be able to detect EMRBs originating from the Virgo cluster^[67], however the detectable rate may be only $1 \times 10^{-4} \text{ yr}^{-1}$ per galaxy^[68]. It would be interesting to check what we could expect to infer about MBHs in other galaxies from GWs.

Chapter 4

Future Work

The work outlined in previous chapters should be largely completed by the end of 2010. It may be that further investigation reveals additional avenues to explore; however, it will be necessary to find new projects as well. Development of new areas of study will depend upon what is presented in the literature in the intervening time. Current ideas are discussed below.

4.1 Other Theories Of Gravity

Analysis similar to that discussed in chapter 2 for metric $f(R)$ gravity may be performed for other theories of modified gravity. This is a rapidly developing area incorporating ideas from quantum gravity and cosmology. Other theories to be investigated could include:

- Metric-affine gravity^[19,20], as discussed in section 2.1.1. Since this is not a metric theory of gravity it may be possible to find observational tests that strongly constrain, or rule out this theory^[2].
- Generalised higher-order gravities which replace R in the Einstein-Hilbert action with $f(R, R_{\mu\nu}R^{\mu\nu}, R_{\mu\nu\rho\sigma}R^{\mu\nu\rho\sigma})$ ^[25,105]. We see that $f(R)$ is just a simplification of this case. Again we should recover the results of quadratic gravity in linearized theory^[28,29,38,39,42].
- Hořava-Lifshitz gravity^[106–108] which sacrifices spacetime covariance in favour of being renormalizable. A preferred foliation of space and time along the lines of the Arnowitt-Deser-Misner (ADM) formalism is adopted^[109], with Lorentz invariance being emergent at large distances. This removes many of the problems associated with time traditionally associated with trying to quantize GR.
- Chern-Simons modified gravity^[110] which includes gravitational parity violation. Motivated by gauge theories, Chern-Simons gravity includes a term in the action proportional to the Pontryagin density $*RR = 1/2 \epsilon^{\nu\rho\sigma\tau} R^\lambda_{\mu\sigma\tau} R^\mu_{\lambda\nu\rho}$, where $\epsilon^{\nu\rho\sigma\tau}$ is the Levi-Civita alternating tensor, coupled to a (pseudo-)scalar field ϑ . Consequences of this include birefringent GWs, altered precession rates, and

the modification of vacuum solutions that are axisymmetric but not spherically symmetric such as Kerr.

Since there are so many ways to formulate an alternate theory of gravity, there are many opportunities for study in this area. It would be desirable to find tests that can distinguish these theories from each other and GR; strong-field tests seem the most promising.

4.2 Observing Black Hole Shadows

Black holes are intriguing objects. In the next few years it is hoped that VLBI will advance to the stage that it will be possible to resolve features of the size of the order of the event horizon for sufficiently massive galactic BHs^[96]. Due to its mass and proximity, Sgr A* is the prime candidate^[111]. This capability would allow us to directly image accretion flows down to the event horizon, and would be the first direct evidence that these compact objects are actually BHs as currently understood, not some other exotic object.

One of the main targets of these strong-field VLBI observations is the measurement of the BH's shadow. This is the dark region surrounding the BH from which no light can reach the observer; it is bounded by the innermost photon orbit^[64]. The exact shape of the shadow is intimately linked to the metric and is a sensitive probe of the spacetime. By measuring the shape of the shadow it may be possible to measure the spin and inclination of the BH^[112], assuming it is Kerr, check whether it is an over-extreme Kerr BH^[113], or even probe deviations from Kerr^[114, 115]. It would be interesting to investigate the shape of the shadow in other spacetimes, for example Manko-Novikov^[49, 116] which form a family of exact asymptotically flat spacetimes with arbitrary multipole moments. The shape of the shadow of a Kerr BH is shown in figure 4.1. The shadow remains near circular for spin values $a \lesssim 0.9M_\bullet$ regardless of inclination (axisymmetry requires that the shadow is circular when looking along the rotation axis) even though the Kerr spacetime is highly non-spherically symmetric^[115]. Observing deviations from Kerr would disprove the no-hair theorem (possibly admitting naked singularities), provide evidence for a non-GR theory of gravity, or both. In order to do so it will be necessary to find a convenient parameterization to describe the shape of the shadow.

Acknowledgements I am grateful to Jonathan Gair for suggesting this work presented here, for many helpful conversations and for his careful checking of minus signs. I would also like to thank Dave Green for his suggestions regarding apodization.

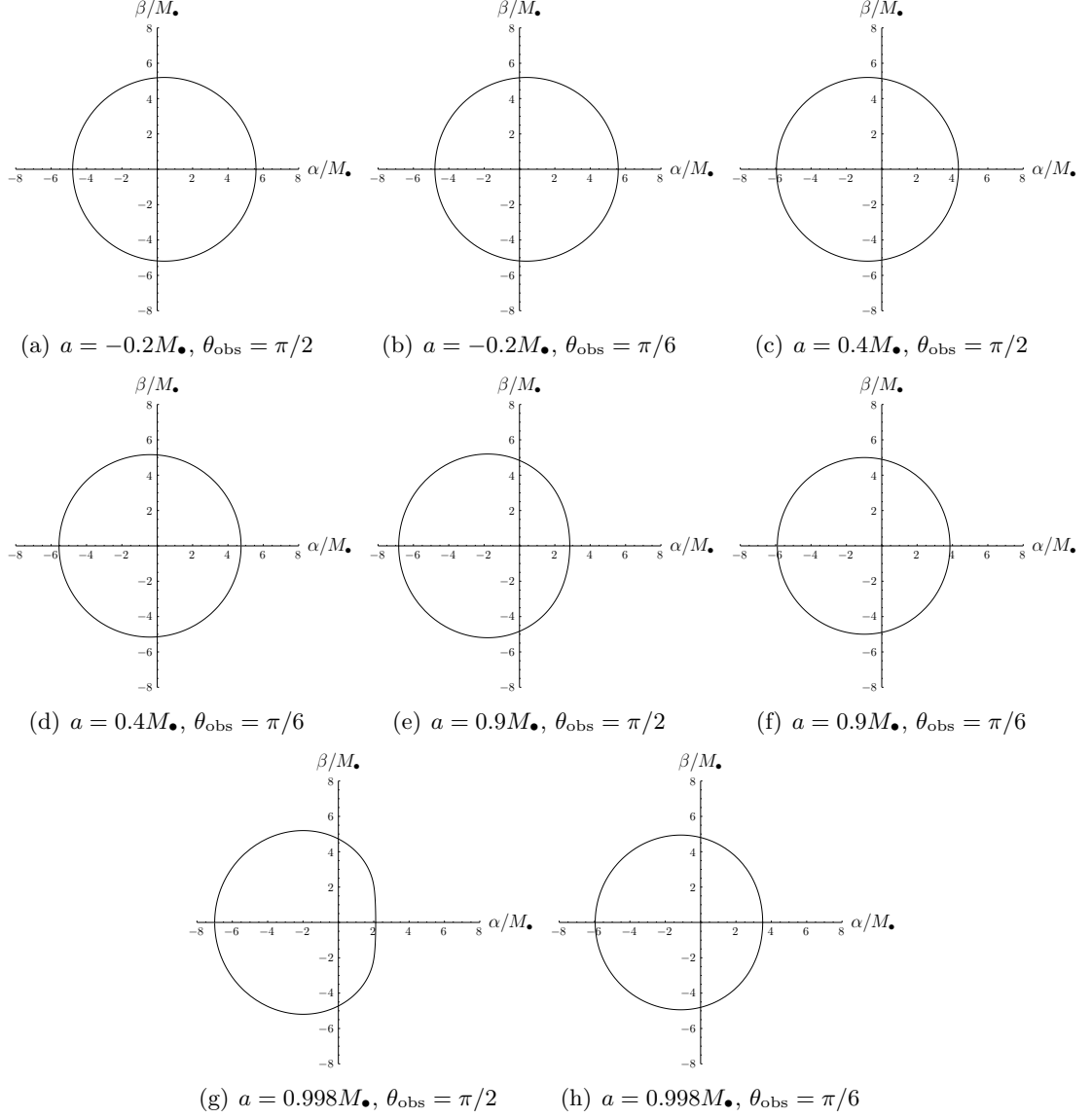


Figure 4.1: Apparent shape of the shadow of a Kerr BH viewed at infinity. α and β are the position coordinates projected onto the celestial sphere, and θ_{obs} is the polar coordinate of the observer^[64]. If $\theta_{\text{obs}} = 0, \pi$ we would be looking along the spin axis and would see a circular shadow.

References

- [1] Misner, C. W., Thorne, K. S. & Wheeler, J. A.; *Gravitation*; New York: W. H. Freeman, 1973.
- [2] Will, C. M.; *Living Reviews in Relativity*; **9**(3); 2006.
- [3] Stairs, I. H.; *Living Reviews in Relativity*; **6**(5); 2003.
- [4] Abramovici, A., Althouse, W. E., Drever, R. W. P. *et al.*; *Science*; **256**(5055):325–333; 1992.
- [5] Abbott, B. P., Abbott, R., Adhikari, R. *et al.*; *Reports on Progress in Physics*; **72**(7):076901(25); 2009.
- [6] Accadia, T., Acernese, F., Antonucci, F. *et al.*; *Journal of Physics: Conference Series*; **203**(1):012074; 2010.
- [7] Bender, P., Brillet, A., Ciufolini, I. *et al.*; LISA Pre-Phase A Report; 1998.
- [8] Danzmann, K. & Rüdiger, A.; *Classical and Quantum Gravity*; **20**(10):S1–S9; 2003.
- [9] Psaltis, D., Perrodin, D., Dienes, K. R. & Mocioiu, I.; *Physical Review Letters*; **100**(9):091101(4); 2008.
- [10] Landau, L. D. & Lifshitz, E. M.; *The Classical Theory of Fields*; fourth edition; Course of Theoretical Physics; Oxford: Butterworth-Heinemann, 1975.
- [11] Sotiriou, T. P. & Faraoni, V.; *Reviews of Modern Physics*; **82**(1):451–497; 2010.
- [12] De Felice, A. & Tsujikawa, S.; *Living Reviews in Relativity*; **13**(3); 2010.
- [13] Buchdahl, H. A.; *Monthly Notices of the Royal Astronomical Society*; **150**:1–8; 1970.
- [14] Park, M., Zurek, K. M. & Watson, S.; *Physical Review D*; **81**(12):124008(18); 2010.
- [15] Exirifard, Q. & Sheik-Jabbari, M.; *Physics Letters B*; **661**(2-3):158–161; 2008.
- [16] Lovelock, D.; *Aequationes Mathematicae*; **4**(1-2):127–138; 1970.
- [17] Lovelock, D.; *Journal of Mathematical Physics*; **12**(3):498; 1971.
- [18] Lovelock, D.; *Journal of Mathematical Physics*; **13**(6):874; 1972.
- [19] Sotiriou, T. & Liberati, S.; *Annals of Physics*; **322**(4):935–966; 2007.
- [20] Sotiriou, T. P. & Liberati, S.; *Journal of Physics: Conference Series*; **68**:012022(7); 2007.
- [21] Barausse, E., Sotiriou, T. P. & Miller, J. C.; *Classical and Quantum Gravity*; **25**(6):062001(7); 2008.

- [22] Barausse, E., Sotiriou, T. P. & Miller, J. C.; *Classical and Quantum Gravity*; **25**(10):105008(15); 2008.
- [23] York, J., James W.; *Physical Review Letters*; **28**(16):1082–1085; 1972.
- [24] Gibbons, G. W. & Hawking, S. W.; *Physical Review D*; **15**(10):2752–2756; 1977.
- [25] Madsen, M. S. & Barrow, J. D.; *Nuclear Physics B*; **323**(1):242–252; 1989.
- [26] Dyer, E. & Hinterbichler, K.; *Physical Review D*; **79**(2):024028; 2009.
- [27] Koivisto, T.; *Classical and Quantum Gravity*; **23**(12):4289–4296; 2006.
- [28] Schmidt, H.-J.; *Astronomische Nachrichten: A Journal on all Fields of Astronomy*; **307**(5):339–340; 1986.
- [29] Teyssandier, P.; *Astronomische Nachrichten: A Journal on all Fields of Astronomy*; **311**(4):209–212; 1990.
- [30] Olmo, G. J.; *Physical Review Letters*; **95**(26):261102(4); 2005.
- [31] Corda, C.; *International Journal of Modern Physics A*; **23**(10):1521–1535; 2007.
- [32] Hobson, M. P., Efstathiou, G. & Lasenby, A.; *General Relativity: An Introduction for Physicists*; Cambridge: Cambridge University Press, 2006.
- [33] Capozziello, S., Corda, C. & De Laurentis, M.; *Physics Letters B*; **669**(5):255–259; 2008.
- [34] Peskin, M. E. & Schroeder, D. V.; *An Introduction to Quantum Field Theory*; Boulder, Colorado: Westview Press, 1995.
- [35] Capozziello, S., Stabile, A. & Troisi, A.; *Modern Physics Letters A*; **24**(09):659–665; 2009.
- [36] Näf, J. & Jetzer, P.; *Physical Review D*; **81**(10):104003(8); 2010.
- [37] Chiba, T., Smith, T. & Erickcek, A.; *Physical Review D*; **75**(12):124014(7); 2007.
- [38] Pechlaner, E. & Sexl, R.; *Communications in Mathematical Physics*; **2**(1):165–175; 1966.
- [39] Stelle, K. S.; *General Relativity and Gravitation*; **9**(4):353–371; 1978.
- [40] Barausse, E. & Sotiriou, T. P.; *Physical Review Letters*; **101**(9):099001(1); 2008.
- [41] Olmo, G. J.; *Physical Review D*; **75**(2):023511(8); 2007.
- [42] Capozziello, S. & Stabile, A.; *Classical and Quantum Gravity*; **26**(8):085019(22); 2009.
- [43] Adelberger, E., Gundlach, J., Heckel, B. *et al.*; *Progress in Particle and Nuclear Physics*; **62**(1):102–134; 2009.
- [44] Adelberger, E., Heckel, B. & Nelson, A.; *Annual Review of Nuclear and Particle Science*; **53**(1):77–121; 2003.
- [45] Kapner, D., Cook, T., Adelberger, E. *et al.*; *Physical Review Letters*; **98**(2):021101; 2007.
- [46] Hoyle, C., Kapner, D., Heckel, B. *et al.*; *Physical Review D*; **70**(4):042004(31); 2004.
- [47] Bertotti, B., Iess, L. & Tortora, P.; *Nature*; **425**(6956):374–376; 2003.
- [48] Hinshaw, G., Weiland, J. L., Hill, R. S. *et al.*; *The Astrophysical Journal Supplement Series*; **180**(2):225–245; 2009.

-
- [49] Gair, J., Li, C. & Mandel, I.; *Physical Review D*; **77**(2):024035(23); 2008.
 - [50] Kerner, R., van Holten, J. W. & Colistete, J., R.; *Classical and Quantum Gravity*; **18**(22):4725–4742; 2001.
 - [51] Cox, A. N.; *Allen’s Astrophysical Quantities*; fourth edition; New York: Springer-Verlag, 2000.
 - [52] Pitjeva, E. V.; EPM ephemerides and relativity; in Klioner, S. A., Seidelmann, P. K. & Soffel, M. H. (editors), *Proceedings of the International Astronomical Union*; volume 5; 170–178; Cambridge: Cambridge University Press, 2009.
 - [53] Khoury, J. & Weltman, A.; *Physical Review Letters*; **93**(17):171104(4); 2004.
 - [54] Khoury, J. & Weltman, A.; *Physical Review D*; **69**(4):044026(15); 2004.
 - [55] Corda, C.; *The European Physical Journal C*; **65**(1-2):257–267; 2009.
 - [56] Lynden-Bell, D. & Rees, M. J.; *Monthly Notices of the Royal Astronomical Society*; **152**; 1971.
 - [57] Rees, M. J.; *Annual Review of Astronomy and Astrophysics*; **22**(1):471–506; 1984.
 - [58] Gillessen, S., Eisenhauer, F., Trippe, S. *et al.*; *The Astrophysical Journal*; **692**(2):1075–1109; 2009.
 - [59] Israel, W.; *Physical Review*; **164**(5):1776–1779; 1967.
 - [60] Israel, W.; *Communications in Mathematical Physics*; **8**(3):245–260; 1968.
 - [61] Carter, B.; *Physical Review Letters*; **26**(6):331–333; 1971.
 - [62] Hawking, S. W.; *Communications in Mathematical Physics*; **25**(2):152–166; 1972.
 - [63] Robinson, D.; *Physical Review Letters*; **34**(14):905–906; 1975.
 - [64] Chandrasekhar, S.; *The Mathematical Theory of Black Holes*; Oxford Classic Texts in the Physical Sciences; Oxford: Oxford University Press, 1998.
 - [65] Merritt, D., Mikkola, S. & Will, C. M.; *Physical Review D*; **81**(6):062002(17); 2010.
 - [66] Kato, Y., Miyoshi, M., Takahashi, R. *et al.*; *Monthly Notices of the Royal Astronomical Society: Letters*; **403**(1):L74–L78; 2010.
 - [67] Rubbo, L. J., Holley-Bockelmann, K. & Finn, L. S.; *The Astrophysical Journal*; **649**(1):L25–L28; 2006.
 - [68] Hopman, C., Freitag, M. & Larson, S. L.; *Monthly Notices of the Royal Astronomical Society*; **378**(1):129–136; 2007.
 - [69] Kobayashi, S., Laguna, P., Phinney, E. S. & Meszaros, P.; *The Astrophysical Journal*; **615**(2):855–865; 2004.
 - [70] Babak, S., Fang, H., Gair, J. *et al.*; *Physical Review D*; **75**(2):024005(25); 2007.
 - [71] Kerr, R.; *Physical Review Letters*; **11**(5):237–238; 1963.
 - [72] Boyer, R. H. & Lindquist, R. W.; *Journal of Mathematical Physics*; **8**(2):265–281; 1967.
 - [73] Carter, B.; *Physical Review*; **174**(5):1559–1571; 1968.
 - [74] de Felice, F.; *Journal of Physics A: Mathematical and General*; **13**(5):1701–1708; 1980.
-

-
- [75] Rosquist, K., Bylund, T. & Samuelsson, L.; *International Journal of Modern Physics D*; **18**(03):429–434; 2009.
 - [76] Wilkins, D.; *Physical Review D*; **5**(4):814–822; 1972.
 - [77] Drasco, S. & Hughes, S.; *Physical Review D*; **69**(4):044015(11); 2004.
 - [78] Gair, J., Kennefick, D. & Larson, S.; *Physical Review D*; **72**(8):084009(20); 2005.
 - [79] Glampedakis, K. & Kennefick, D.; *Physical Review D*; **66**(4):044002(33); 2002.
 - [80] Ruffini, R. & Sasaki, M.; *Progress of Theoretical Physics*; **66**(5):1627–1638; 1981.
 - [81] Press, W.; *Physical Review D*; **15**(4):965–968; 1977.
 - [82] Bekenstein, J. D.; *The Astrophysical Journal*; **183**:657; 1973.
 - [83] Cutler, C.; *Physical Review D*; **57**(12):7089–7102; 1998.
 - [84] Finn, L. S.; *Physical Review D*; **46**(12):5236–5249; 1992.
 - [85] Cutler, C., Kennefick, D. & Poisson, E.; *Physical Review D*; **50**(6):3816–3835; 1994.
 - [86] Barack, L. & Cutler, C.; *Physical Review D*; **69**(8):082005(24); 2004.
 - [87] Jones, N. B. (editor); *Digital Signal Processing*; IEE Control Engineering Series; Exeter: Peter Peregrinus, 1982.
 - [88] Harris, F.; *Proceedings of the IEEE*; **66**(1):51–83; 1978.
 - [89] Kaiser, J. & Schafer, R.; *Acoustics, Speech and Signal Processing, IEEE Transactions on*; **28**(1):105–107; 1980.
 - [90] Nuttall, A.; *IEEE Transactions on Acoustics, Speech and Signal Processing*; **29**(1):84–91; 1981.
 - [91] Ghez, A. M., Salim, S., Weinberg, N. N. *et al.*; *The Astrophysical Journal*; **689**(2):1044–1062; 2008.
 - [92] Thorne, K. S.; *The Astrophysical Journal*; **191**(2):507–519; 1974.
 - [93] King, A. R. & Pringle, J. E.; *Monthly Notices of the Royal Astronomical Society: Letters*; **373**(1):L90–L92; 2006.
 - [94] King, A. R., Pringle, J. E. & Hofmann, J. A.; *Monthly Notices of the Royal Astronomical Society*; **385**(3):1621–1627; 2008.
 - [95] Reid, M. J., Menten, K. M., Genzel, R. *et al.*; *Astronomische Nachrichten*; **324**(S1):505–511; 2003.
 - [96] Doleman, S. S., Weintroub, J., Rogers, A. E. E. *et al.*; *Nature*; **455**(7209):78–80; 2008.
 - [97] Reid, M. J., Readhead, A. C. S., Vermeulen, R. C. & Treuhaft, R. N.; *The Astrophysical Journal*; **524**(2):816–823; 1999.
 - [98] Backer, D. C. & Sramek, R. A.; *The Astrophysical Journal*; **524**(2):805–815; 1999.
 - [99] Jaynes, E. T.; *Probability Theory: The Logic of Science*; Cambridge: Cambridge University Press, 2003.
 - [100] Vallisneri, M.; *Physical Review D*; **77**(4):042001(20); 2008.
 - [101] Peters, P. C. & Mathews, J.; *Physical Review*; **131**(1):435–440; 1963.
-

- [102] Peters, P. C.; *Physical Review*; **136**(4B):B1224–B1232; 1964.
- [103] Gair, J. R.; private communication; 2010.
- [104] Watson, G. N.; *A Treatise on the Theory of Bessel Functions*; second edition; Cambridge Mathematical Library; Cambridge: Cambridge University Press, 1995.
- [105] Farhoudi, M.; *General Relativity and Gravitation*; **38**(8):1261–1284; 2006.
- [106] Hořava, P.; *Physical Review D*; **79**(8):084008(15); 2009.
- [107] Blas, D., Pujolàs, O. & Sibiryakov, S.; *Physical Review Letters*; **104**(18):181302(4); 2010.
- [108] Sotiriou, T. P., Visser, M. & Weinfurtner, S.; *Journal of High Energy Physics*; **2009**(10):033(32); 2009.
- [109] Arnowitt, R., Deser, S. & Misner, C. W.; The Dynamics of General Relativity; in Witten, L. (editor), *Gravitation: an introduction to current research*; chapter 7, 227–264; New York: Wiley, 1962.
- [110] Alexander, S. & Yunes, N.; *Physics Reports*; **480**(1-2):1–55; 2009.
- [111] Broderick, A. E., Loeb, A. & Narayan, R.; *The Astrophysical Journal*; **701**(2):1357–1366; 2009.
- [112] Hioki, K. & Maeda, K.; *Physical Review D*; **80**(2):024042(9); 2009.
- [113] Bambi, C. & Freese, K.; *Physical Review D*; **79**(4):043002(7); 2009.
- [114] Johannsen, T. & Psaltis, D.; *The Astrophysical Journal*; **716**(1):187–197; 2010.
- [115] Johannsen, T. & Psaltis, D.; *The Astrophysical Journal*; **718**(1):446–454; 2010.
- [116] Manko, V. S. & Novikov, I. D.; *Classical and Quantum Gravity*; **9**(11):2477; 1992.

Appendix A

Inverse Fisher Matrix Elements

The following tables give the inverse Fisher matrix elements for a small selection of example orbits. The values are normalised with respect to their maximum-likelihood values, thus $(F^{-1})_{aa} = 1 \times 10^{-4}$ indicates that the uncertainty in parameter λ^a is 1 %. The inverse Fisher matrix elements only use information from the gravitational wave. They do not make use of any other prior information, such as results from other observations. They are therefore an upper bound on the size of the posterior variance: we will be able to infer parameters more accurately if we combine all the information we have regarding them.

	M_\bullet	a	Θ	Ψ	$\bar{\Theta}$	$\bar{\Phi}$	L_z	Q	μ	x_0	y_0	z_0
M_\bullet	2.7E-04	-8.4E-06	-3.0E-06	9.1E-05	8.1E-05	9.4E-06	3.0E-05	3.8E-06	7.1E-04	2.8E-05	1.9E-04	-2.2E-05
a	-8.4E-06	1.9E-03	-4.5E-04	4.2E-04	4.9E-04	-4.7E-04	-4.3E-05	1.0E-04	1.3E-04	1.2E-05	-2.7E-06	-1.6E-04
Θ	-3.0E-06	-4.5E-04	7.7E-04	5.4E-04	-3.5E-04	-4.8E-05	6.1E-05	-2.9E-04	4.4E-04	-9.9E-06	-2.3E-05	-2.9E-05
Ψ	9.1E-05	4.2E-04	5.4E-04	9.9E-03	-1.5E-03	-3.1E-03	-6.7E-04	-1.4E-04	-4.3E-03	3.9E-05	-2.6E-04	-2.9E-04
$\bar{\Theta}$	8.1E-05	4.9E-04	-3.5E-04	-1.5E-03	1.5E-02	-1.3E-04	1.2E-04	-1.4E-04	2.9E-02	-2.8E-05	1.7E-04	8.6E-05
$\bar{\Phi}$	9.4E-06	-4.7E-04	-4.8E-05	-3.1E-03	-1.3E-04	2.1E-03	3.9E-05	-4.7E-05	-2.8E-04	9.8E-07	1.2E-05	7.0E-05
L_z	3.0E-05	-4.3E-05	6.1E-05	-6.7E-04	1.2E-04	3.9E-05	2.2E-04	-9.8E-06	1.1E-03	3.5E-05	1.6E-05	1.4E-05
Q	3.8E-06	1.0E-04	-2.9E-04	-1.4E-04	-1.4E-04	-4.7E-05	-9.8E-06	9.4E-04	-1.2E-04	-3.3E-06	1.8E-05	-6.4E-04
μ	7.1E-04	1.3E-04	4.4E-04	-4.3E-03	2.9E-02	-2.8E-04	1.1E-03	-1.2E-04	8.3E-02	1.1E-04	6.8E-04	-3.4E-04
x_0	2.8E-05	1.2E-05	-9.9E-06	3.9E-05	-2.8E-05	9.8E-07	3.5E-05	-3.3E-06	1.1E-04	2.4E-04	-1.5E-04	9.8E-06
y_0	1.9E-04	-2.7E-06	-2.3E-05	-2.6E-04	1.7E-04	1.2E-05	1.6E-05	1.8E-05	6.8E-04	-1.5E-04	3.9E-04	-8.0E-06
z_0	-2.2E-05	-1.6E-04	-2.9E-05	-2.9E-04	8.6E-05	7.0E-05	1.4E-05	-6.4E-04	-3.4E-04	9.8E-06	-8.0E-06	1.1E-03

Table A.1: Inverse Fisher matrix elements for the orbit specified in figure 3.6. The periapsis is $r_p = 52.7M_\bullet$, the SNR is $\rho = 4.6$.

	M_\bullet	a	Θ	Ψ	$\bar{\Theta}$	$\bar{\Phi}$	L_z	Q	μ	x_0	y_0	z_0
M_\bullet	8.8E-12	1.9E-13	3.0E-15	-6.1E-14	8.4E-14	3.2E-14	3.0E-16	-2.0E-12	-2.3E-14	-8.6E-12	1.4E-16	1.0E-12
a	1.9E-13	5.8E-08	2.7E-10	-1.4E-08	2.5E-08	8.6E-09	1.2E-10	-5.8E-07	3.1E-10	-7.7E-13	7.7E-14	2.9E-07
Θ	3.0E-15	2.7E-10	8.6E-11	9.9E-10	3.6E-10	-1.9E-10	-9.0E-12	-3.4E-09	3.9E-10	-1.0E-14	6.6E-16	1.2E-09
Ψ	-6.1E-14	-1.4E-08	9.9E-10	4.3E-08	1.2E-09	-1.1E-08	-1.8E-10	1.3E-07	1.2E-08	2.5E-13	-2.4E-14	-7.8E-08
$\bar{\Theta}$	8.4E-14	2.5E-08	3.6E-10	1.2E-09	1.8E-08	2.3E-09	1.5E-11	-2.7E-07	8.1E-09	-3.4E-13	3.2E-14	1.3E-07
$\bar{\Phi}$	3.2E-14	8.6E-09	-1.9E-10	-1.1E-08	2.3E-09	3.5E-09	4.7E-11	-8.4E-08	-3.2E-09	-1.3E-13	1.2E-14	4.6E-08
L_z	3.0E-16	1.2E-10	-9.0E-12	-1.8E-10	1.5E-11	4.7E-11	8.5E-12	-9.4E-10	3.0E-11	-1.6E-15	2.0E-16	4.9E-10
Q	-2.0E-12	-5.8E-07	-3.4E-09	1.3E-07	-2.7E-07	-8.4E-08	-9.4E-10	6.1E-06	3.3E-08	8.0E-12	-7.7E-13	-3.1E-06
μ	-2.3E-14	3.1E-10	3.9E-10	1.2E-08	8.1E-09	-3.2E-09	3.0E-11	3.3E-08	3.3E-08	2.9E-14	7.0E-15	-2.8E-08
x_0	-8.6E-12	-7.7E-13	-1.0E-14	2.5E-13	-3.4E-13	-1.3E-13	-1.6E-15	8.0E-12	2.9E-14	3.2E-11	-1.2E-15	-4.1E-12
y_0	1.4E-16	7.7E-14	6.6E-16	-2.4E-14	3.2E-14	1.2E-14	2.0E-16	-7.7E-13	7.0E-15	-1.2E-15	2.4E-11	3.9E-13
z_0	1.0E-12	2.9E-07	1.2E-09	-7.8E-08	1.3E-07	4.6E-08	4.9E-10	-3.1E-06	-2.8E-08	-4.1E-12	3.9E-13	1.6E-06

Table A.2: Inverse Fisher matrix elements for the orbit specified in figure 3.7. The periapsis is $r_p = 4.67M_\bullet$, the SNR is $\rho = 8800$.

	M_\bullet	a	Θ	Ψ	$\bar{\Theta}$	$\bar{\Phi}$	L_z	Q	μ	x_0	y_0	z_0
M_\bullet	1.1E-07	7.4E-09	1.1E-08	1.2E-07	1.0E-08	-1.8E-08	-5.3E-09	1.1E-08	3.4E-08	-2.8E-08	-1.2E-08	-1.9E-08
a	7.4E-09	2.8E-05	2.1E-07	-1.8E-08	1.1E-07	-6.5E-08	-1.8E-08	2.8E-05	3.9E-06	-4.6E-09	-9.1E-10	-1.0E-05
Θ	1.1E-08	2.1E-07	7.6E-07	3.6E-06	1.8E-07	-5.6E-07	6.4E-08	1.7E-07	1.1E-06	-5.3E-09	-2.1E-09	-9.1E-07
Ψ	1.2E-07	-1.8E-08	3.6E-06	5.5E-05	4.2E-06	-1.1E-05	-3.8E-06	1.9E-06	1.4E-05	-6.0E-08	-2.3E-08	-8.7E-06
$\bar{\Theta}$	1.0E-08	1.1E-07	1.8E-07	4.2E-06	1.7E-05	-6.2E-07	-5.0E-07	7.1E-07	2.9E-05	-5.3E-09	-2.1E-09	1.7E-07
$\bar{\Phi}$	-1.8E-08	-6.5E-08	-5.6E-07	-1.1E-05	-6.2E-07	3.2E-06	5.9E-07	-6.4E-07	-2.9E-06	9.3E-09	3.7E-09	2.6E-06
L_z	-5.3E-09	-1.8E-08	6.4E-08	-3.8E-06	-5.0E-07	5.9E-07	6.0E-07	-1.2E-07	-9.8E-07	3.3E-09	1.3E-09	5.1E-07
Q	1.1E-08	2.8E-05	1.7E-07	1.9E-06	7.1E-07	-6.4E-07	-1.2E-07	5.0E-05	7.3E-06	-6.6E-09	-1.5E-09	1.5E-05
μ	3.4E-08	3.9E-06	1.1E-06	1.4E-05	2.9E-05	-2.9E-06	-9.8E-07	7.3E-06	7.2E-05	-1.8E-08	-6.8E-09	1.8E-07
x_0	-2.8E-08	-4.6E-09	-5.3E-09	-6.0E-08	-5.3E-09	9.3E-09	3.3E-09	-6.6E-09	-1.8E-08	1.4E-07	-5.0E-08	9.8E-09
y_0	-1.2E-08	-9.1E-10	-2.1E-09	-2.3E-08	-2.1E-09	3.7E-09	1.3E-09	-1.5E-09	-6.8E-09	-5.0E-08	1.3E-07	3.6E-09
z_0	-1.9E-08	-1.0E-05	-9.1E-07	-8.7E-06	1.7E-07	2.6E-06	5.1E-07	1.5E-05	1.8E-07	9.8E-09	3.6E-09	6.3E-05

Table A.3: Inverse Fisher matrix elements for the orbit specified in figure 3.8. The periapsis is $r_p = 11.77M_\bullet$, the SNR is $\rho = 140$.

	M_\bullet	a	Θ	Ψ	$\bar{\Theta}$	$\bar{\Phi}$	L_z	Q	μ	x_0	y_0	z_0
M_\bullet	6.1E-04	-6.8E-04	-3.8E-05	-2.3E-03	-1.6E-04	7.4E-04	1.8E-05	-1.6E-05	5.3E-04	1.2E-04	3.6E-04	1.1E-05
a	-6.8E-04	5.2E-02	-3.9E-04	4.2E-02	9.5E-04	-1.5E-02	1.3E-03	-2.2E-03	1.7E-02	-3.3E-04	2.7E-04	-2.3E-04
Θ	-3.8E-05	-3.9E-04	1.5E-03	2.5E-03	2.2E-03	-8.5E-04	8.3E-05	-2.0E-04	4.2E-03	5.2E-05	-6.0E-05	-3.0E-04
Ψ	-2.3E-03	4.2E-02	2.5E-03	1.6E-01	1.3E-02	-5.5E-02	4.8E-03	-6.8E-05	7.0E-02	-1.5E-03	1.8E-03	-9.2E-04
$\bar{\Theta}$	-1.6E-04	9.5E-04	2.2E-03	1.3E-02	1.5E-01	-3.9E-03	9.0E-04	7.8E-06	1.9E-01	1.2E-04	8.8E-05	-2.9E-04
$\bar{\Phi}$	7.4E-04	-1.5E-02	-8.5E-04	-5.5E-02	-3.9E-03	2.0E-02	-1.5E-03	-5.4E-05	-2.3E-02	4.9E-04	-5.8E-04	4.1E-04
L_z	1.8E-05	1.3E-03	8.3E-05	4.8E-03	9.0E-04	-1.5E-03	4.4E-04	9.6E-05	3.8E-03	6.1E-05	1.4E-05	-1.9E-04
Q	-1.6E-05	-2.2E-03	-2.0E-04	-6.8E-05	7.8E-06	-5.4E-05	9.6E-05	2.0E-03	2.6E-04	1.9E-05	-3.1E-05	-1.3E-03
μ	5.3E-04	1.7E-02	4.2E-03	7.0E-02	1.9E-01	-2.3E-02	3.8E-03	2.6E-04	3.0E-01	2.5E-04	1.3E-03	-2.2E-03
x_0	1.2E-04	-3.3E-04	5.2E-05	-1.5E-03	1.2E-04	4.9E-04	6.1E-05	1.9E-05	2.5E-04	6.8E-04	-4.3E-04	2.8E-05
y_0	3.6E-04	2.7E-04	-6.0E-05	1.8E-03	8.8E-05	-5.8E-04	1.4E-05	-3.1E-05	1.3E-03	-4.3E-04	8.6E-04	-3.8E-05
z_0	1.1E-05	-2.3E-04	-3.0E-04	-9.2E-04	-2.9E-04	4.1E-04	-1.9E-04	-1.3E-03	-2.2E-03	2.8E-05	-3.8E-05	2.1E-03

Table A.4: Inverse Fisher matrix elements for the orbit specified in figure 3.9. The periapsis is $r_p = 53.7M_\bullet$, the SNR is $\rho = 2.2$.

	M_\bullet	a	Θ	Ψ	$\bar{\Theta}$	$\bar{\Phi}$	L_z	Q	μ	x_0	y_0	z_0
M_\bullet	9.3E-06	6.4E-08	-1.3E-07	2.6E-06	-3.5E-07	-9.0E-08	6.9E-07	6.8E-08	5.8E-07	-1.1E-06	1.6E-06	8.1E-06
a	6.4E-08	2.3E-05	2.0E-07	9.8E-06	-9.7E-07	-4.2E-06	-3.1E-07	2.9E-06	2.6E-07	6.0E-08	-1.0E-07	4.5E-08
Θ	-1.3E-07	2.0E-07	1.4E-05	3.4E-05	-1.9E-06	-2.4E-06	-8.5E-06	-3.7E-06	-3.7E-05	1.2E-06	-7.4E-07	-3.6E-07
Ψ	2.6E-06	9.8E-06	3.4E-05	2.6E-04	-2.4E-05	-4.0E-05	8.2E-06	-2.2E-06	-3.1E-05	6.6E-08	4.3E-07	-1.2E-06
$\bar{\Theta}$	-3.5E-07	-9.7E-07	-1.9E-06	-2.4E-05	1.6E-04	-6.1E-07	-2.7E-06	1.4E-06	3.0E-04	-1.8E-08	6.2E-08	-5.8E-08
$\bar{\Phi}$	-9.0E-08	-4.2E-06	-2.4E-06	-4.0E-05	-6.1E-07	2.2E-05	1.2E-06	-1.2E-06	-8.2E-08	8.8E-09	-6.4E-08	1.1E-07
L_z	6.9E-07	-3.1E-07	-8.5E-06	8.2E-06	-2.7E-06	1.2E-06	1.7E-05	-6.7E-06	4.8E-05	-6.7E-07	5.2E-07	4.8E-07
Q	6.8E-08	2.9E-06	-3.7E-06	-2.2E-06	1.4E-06	-1.2E-06	-6.7E-06	2.6E-05	-5.3E-06	-5.6E-07	3.3E-07	-1.8E-07
μ	5.8E-07	2.6E-07	-3.7E-05	-3.1E-05	3.0E-04	-8.2E-08	4.8E-05	-5.3E-06	9.5E-04	-4.0E-06	3.0E-06	1.5E-07
x_0	-1.1E-06	6.0E-08	1.2E-06	6.6E-08	-1.8E-08	8.8E-09	-6.7E-07	-5.6E-07	-4.0E-06	8.2E-06	-8.7E-06	2.3E-06
y_0	1.6E-06	-1.0E-07	-7.4E-07	4.3E-07	6.2E-08	-6.4E-08	5.2E-07	3.3E-07	3.0E-06	-8.7E-06	1.1E-05	-2.8E-06
z_0	8.1E-06	4.5E-08	-3.6E-07	-1.2E-06	-5.8E-08	1.1E-07	4.8E-07	-1.8E-07	1.5E-07	2.3E-06	-2.8E-06	1.0E-05

Table A.5: Inverse Fisher matrix elements for the orbit specified in figure 3.10. The periapsis is $r_p = 22.7M_\bullet$, the SNR is $\rho = 44$.

	M_\bullet	a	Θ	Ψ	$\bar{\Theta}$	$\bar{\Phi}$	L_z	Q	μ	x_0	y_0	z_0
M_\bullet	1.2E-01	-1.6E-02	-4.1E-04	-1.6E-01	-4.1E-02	1.8E-02	2.0E-02	1.0E-02	-2.7E-01	3.2E-03	9.8E-03	6.2E-03
a	-1.6E-02	5.8E+00	1.7E-01	1.6E+00	2.1E-01	-1.0E+00	-1.1E-02	5.3E-03	4.1E-02	4.6E-02	7.0E-03	3.0E-02
Θ	-4.1E-04	1.7E-01	1.5E-01	3.1E-02	3.3E-02	-7.0E-03	-1.7E-02	2.5E-02	-2.5E-01	2.0E-02	-5.2E-04	-4.6E-03
Ψ	-1.6E-01	1.6E+00	3.1E-02	4.5E+00	-3.6E-01	-1.8E+00	5.1E-02	3.4E-02	-3.6E-01	-5.4E-04	4.6E-02	6.0E-02
$\bar{\Theta}$	-4.1E-02	2.1E-01	3.3E-02	-3.6E-01	8.9E+00	-1.4E-01	1.9E-02	5.8E-03	1.6E+01	-2.2E-03	-1.4E-02	-3.8E-02
$\bar{\Phi}$	1.8E-02	-1.0E+00	-7.0E-03	-1.8E+00	-1.4E-01	1.1E+00	8.7E-04	-1.5E-02	-2.5E-01	1.5E-02	-4.8E-03	-1.3E-02
L_z	2.0E-02	-1.1E-02	-1.7E-02	5.1E-02	1.9E-02	8.7E-04	1.3E-01	1.4E-03	3.9E-01	9.4E-03	-5.0E-03	-1.1E-03
Q	1.0E-02	5.3E-03	2.5E-02	3.4E-02	5.8E-03	-1.5E-02	1.4E-03	1.4E-01	-7.6E-02	-6.6E-03	-4.1E-05	3.1E-02
μ	-2.7E-01	4.1E-02	-2.5E-01	-3.6E-01	1.6E+01	-2.5E-01	3.9E-01	-7.6E-02	4.3E+01	5.3E-02	-6.3E-02	-5.6E-02
x_0	3.2E-03	4.6E-02	2.0E-02	-5.4E-04	-2.2E-03	1.5E-02	9.4E-03	-6.6E-03	5.3E-02	1.4E-01	-2.7E-03	5.2E-03
y_0	9.8E-03	7.0E-03	-5.2E-04	4.6E-02	-1.4E-02	-4.8E-03	-5.0E-03	-4.1E-05	-6.3E-02	-2.7E-03	2.4E-02	-1.0E-03
z_0	6.2E-03	3.0E-02	-4.6E-03	6.0E-02	-3.8E-02	-1.3E-02	-1.1E-03	3.1E-02	-5.6E-02	5.2E-03	-1.0E-03	1.5E-01

Table A.6: Inverse Fisher matrix elements for the orbit specified in figure 3.11. The periapsis is $r_p = 148M_\bullet$, the SNR is $\rho = 0.18$.

